

Response to Anonymous Referee #1

We thank Anonymous Referee #1 for his/her thorough and insightful comments, which are very helpful in our further revision of the manuscript. We have made every effort to address all the concerns raised. Our point-by-point response is given below.

This study presents some detailed observations and complex spectral/wavelet analysis of research aircraft measurements of gravity waves. The waves were observed during START08 and represent a unique dataset to study gravity waves associated with jets. The paper is well structured and provides new insight by quantifying the observed waves – it should be published in ACP. However, I feel that a little extra analysis could make this study more useful, both for quantifying the mesoscale signals and for understanding the wave generation. I suggest the authors consider these extra analyses, which shouldn't be too onerous, in their revised manuscript.

1. Spectral analysis (Figs. 4 and 5).

The authors claim that the spectra reproduce the -5/3 slope, which they do in many cases. However, because of the inherent properties of the spectra this slope is not entirely obvious in many cases, mostly because of the change in slope with scale. I suggest that the authors also complete spectra of kinetic energy (which includes horizontal and vertical velocities), which should show a -5/3 slope extending over more decades (especially in Fig. 5).

Per reviewer's recommendation, we will revise Figure 4 and Figure 5 using Figure R1.01 and Figure R1.02 given in this response below. The composite spectra of kinetic energy can be found in Figure R1.02e. The following sentence will be added in the revision around line 10 on page 4736.

“Even though the kinetic energy spectra (Fig. 5e) may show a -5/3 slope that covers a larger range, the -3 slope over small scale in KE is still evident.”

I can't determine the units of the spectra that are labelled as 'variance' but I assume they are in m^2/s^2 for the velocity components. It would be advantageous to plot the energy density (units of m^3/s^2) instead, which would allow direct comparisons to the cited studies (e.g., Nastrom and Gage 1985, Skamarock 2004).

Strictly speaking, the variance for the velocity components in the current study is “ $m^2 s^{-2} \times \text{unitof}(N) / \text{unitof}(k^*)$ ”. Here, the `unitof()` give the unit of the variable inside the bracket; wavenumber k^* is equal to $\frac{N\Delta x}{\lambda}$; N is the number of points of data in the flight segments; Δx is the spatial resolution of the flight data; λ is the across-track wavelength.

40 In order to use the same unit as those in Nastrom and Gage (1985), all we need to do
41 is simply multiply the current value by Δx . After the modification, the unit will be “
42 $\text{unitof}(\Delta x) \times m^2 s^{-2} \times \text{unitof}(N) / \text{unitof}(k^*) = m^3 s^{-2}$ ”, which is consistent with Nastrom and
43 Gage (1985; their Figure 3). Since Δx is constant ($\Delta x = 250m$), there shouldn't be any
44 change in the spectra slope.

45 Please check the units in the titles of Figure R1.01 and Figure R1.02, which will be
46 replacing the original Figure 4 and Figure 5.

47
48 *2. Inferences about propagation direction*

49
50 *I think the manuscript would benefit from enhanced discussion about what can be inferred about*
51 *horizontal propagation direction and how the superposition of gravity waves propagating in*
52 *opposing directions can complicate the analysis. In particular, around line 20 on p 4739, there is*
53 *discussion of cospectra varying sign. For example as shown in Fig. 7 (leg J3), the cospectra of w*
54 *and p suggest upward propagating waves (almost exclusively). Thus, the variations in sign of the*
55 *cospectra of u and w imply that this track is sampling waves propagating in both the forward*
56 *and backward direction. As argued by the authors (p4740 line ~5) this highlights a difficulty in*
57 *interpreting the waves observed by aircraft, but it does tell us something useful about the wave*
58 *field nonetheless.*

59
60 As suggested, the following sentence will be added in the manuscript around line 21
61 on page 4739.

62 “The variations in the sign of vertical transports of horizontal momentum fluxes
63 imply that this flight segment is sampling waves propagating in both forward and
64 backward direction, assuming the vertical energy transports are generally upward.”

65
66 *For such legs it would be useful to obtain estimates of the net momentum flux. The analysis*
67 *presented could readily separate the averages into positive and negative components, which*
68 *should give a good indication of the dominance of which particular propagation direction as a*
69 *function of scale.*

70
71 The results of net momentum fluxes are shown in Figure R1.03-R1.05, which
72 calculate the cospectrum of $\overline{u'w'}$, $\overline{v'w'}$, and $\overline{w'p_c'}$ based on Fourier transform,
73 respectively. For the scale below ~32 km, both positive values and negative values are
74 important in $\overline{u'w'}$ and $\overline{v'w'}$, while positive $\overline{w'p_c'}$ appears to be more continuous than
75 negative $\overline{w'p_c'}$. For the scale above ~32 km, negative $\overline{u'w'}$ (positive $\overline{w'p_c'}$) appears to be
76 generally more continuous than positive $\overline{u'w'}$ (negative $\overline{w'p_c'}$), while the dominant signs in
77 $\overline{v'w'}$ are generally inconclusive.

78

79 *Similarly, in section 5 – the authors provide detailed analysis of specific example of waves and*
80 *their scales. From this analysis they should be able to infer the (intrinsic) propagation direction*
81 *for each case considered, based on the sign of the cospectra of u and w, and the vertical*
82 *propagation direction. This could be used to comment on the direction of propagation of the*
83 *waves away from any key synoptic features presented in Fig. 2, and whether there is broad*
84 *consistency between these sampled waves and those seen in WRF.*

85
86 **Figure R1.06 in this document demonstrates the comparison between aircraft**
87 **measurements and high-resolution WRF simulations. Preliminary analysis shows that**
88 **WRF successfully captures the variations in wind, potential temperature, and pressure,**
89 **especially for segment J1, J2, J3, and M1. Probably due to upscale error growth with**
90 **relatively long-time integration for segment M2, there is indeed a ~150-km distance**
91 **between the observed V maximum location (at location ~400 km in M2) and the simulated**
92 **one (at location ~550 km in M2). Also, the observed V maximum is larger than the**
93 **simulated one (~60 m/s versus ~50 m/s). With that being said, the forecast error is within a**
94 **reasonable range, and the aircraft did manage to obtain the data within the jet exit region.**

95 **However, it is beyond to the scope of the current study to investigate the**
96 **consistencies and differences between aircraft measurements and WRF. WRF simulations**
97 **and dynamics of the gravity waves will be examined in a separate study. In particular,**
98 **based on the high-resolution simulations, we will investigate the sensitivity of wave**
99 **response to the mean flow speed, wind direction, wind shear, and altitude, as suggested in**
100 **the above comments.**

101
102 *Minor comments:*

103
104 *1. p. 4727 line 15. Suggest changing to: “dominated by signals with sampled periods..” to be*
105 *clear that this isn’t the wave period.*

106
107 **This sentence will be modified in the revision.**

108
109 *2. p. 4730 line 19. I don’t think this claim to be the ‘first’ is entirely correct. It may be the first*
110 *such flight to actually aim to find the mesoscale gravity waves from jet/fronts, but previous*
111 *studies/flights have measured them and analyzed them (e.g., Shapiro and Kennedy 1975; Koch et*
112 *al. 2005).*

113
114 **The sentence in line 19 on page 4730 will be modified as below.**

115 **“The second flight (RF02), which occurred on 21–22 April 2008, was dedicated, to**
116 **our knowledge for the first time, to probing mesoscale gravity waves associated with a**
117 **strong upper-tropospheric jet-front system, even though some previous studies may have**
118 **already measured or analyzed them (e.g., Shapiro and Kennedy 1975; Koch et al. 2005)”**

119
120 *3. To be clear: Do the authors ascertain that the small-scale signals represented in the data are*
121 *entirely fictitious? Or is it that these signals do exist, but the sampling errors (associated with*

122 *the violation of the assumptions about pressure) are very large making the spectral estimates*
123 *unreliable?*

124

125 **With limited observations and accuracy, we cannot ascertain that the small-scale**
126 **signals are entirely fictitious. The current study attempts to argue that small-scale pressure**
127 **could be problematic, and that the small-scale signals may be hard to understand/verify**
128 **using linear theory for propagating monochromatic gravity waves. However, it remains**
129 **possible, though unlikely, some of the small scale variations may be due to nonlinear**
130 **dynamics, shear instability, and/or turbulence that are physical. The below sentences will**
131 **be added to around line 4 on page 4746.**

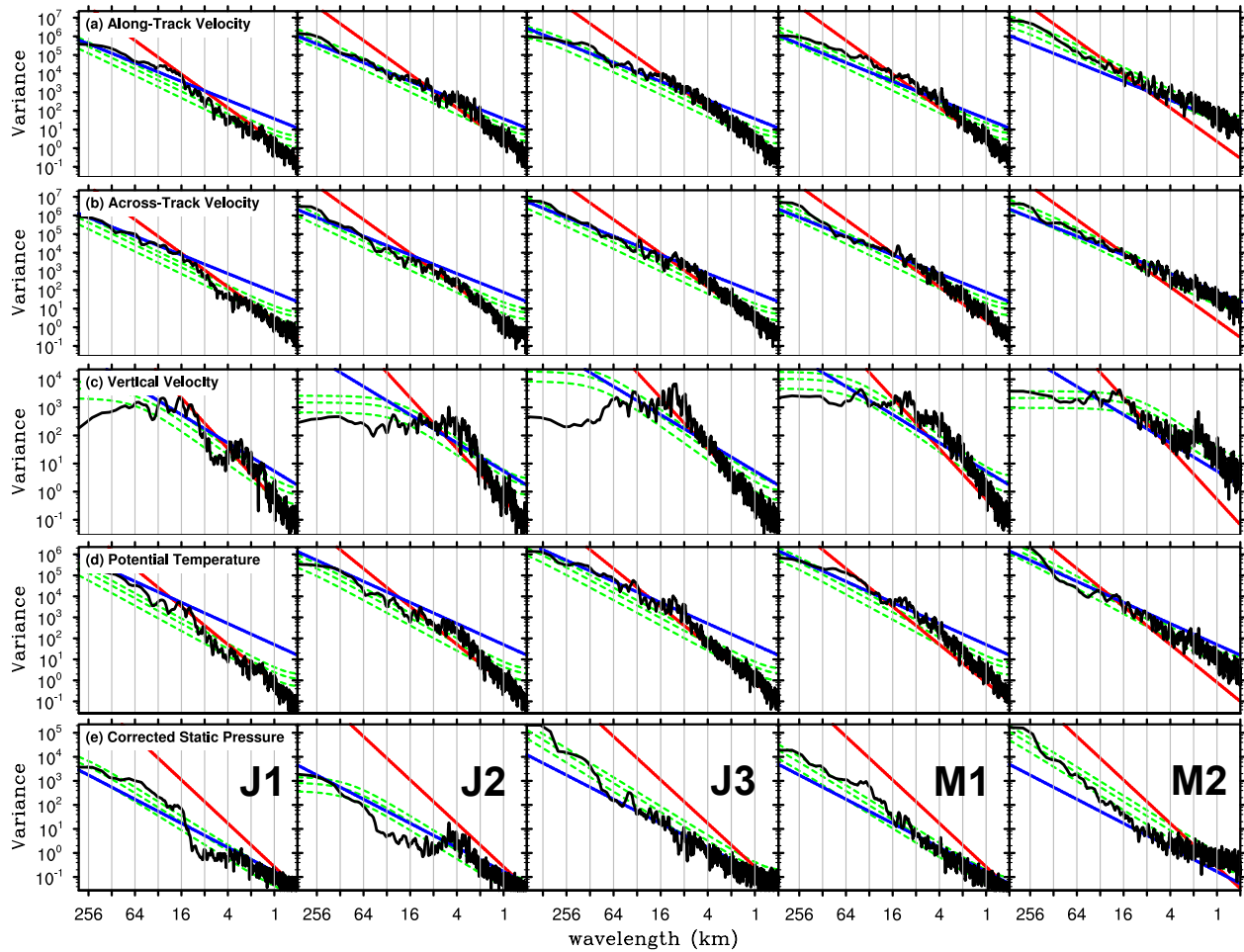
132 **“The current study mainly attempts to verify fluctuations with the use of linear**
133 **theory for monochromatic gravity waves. Therefore, in addition to the measurement error,**
134 **the possibilities that those fluctuations may be due to other physical phenomena (e.g.,**
135 **nonlinear dynamics, shear instability and/or turbulence) cannot be completely ruled out.”**

136

137

138 **References**

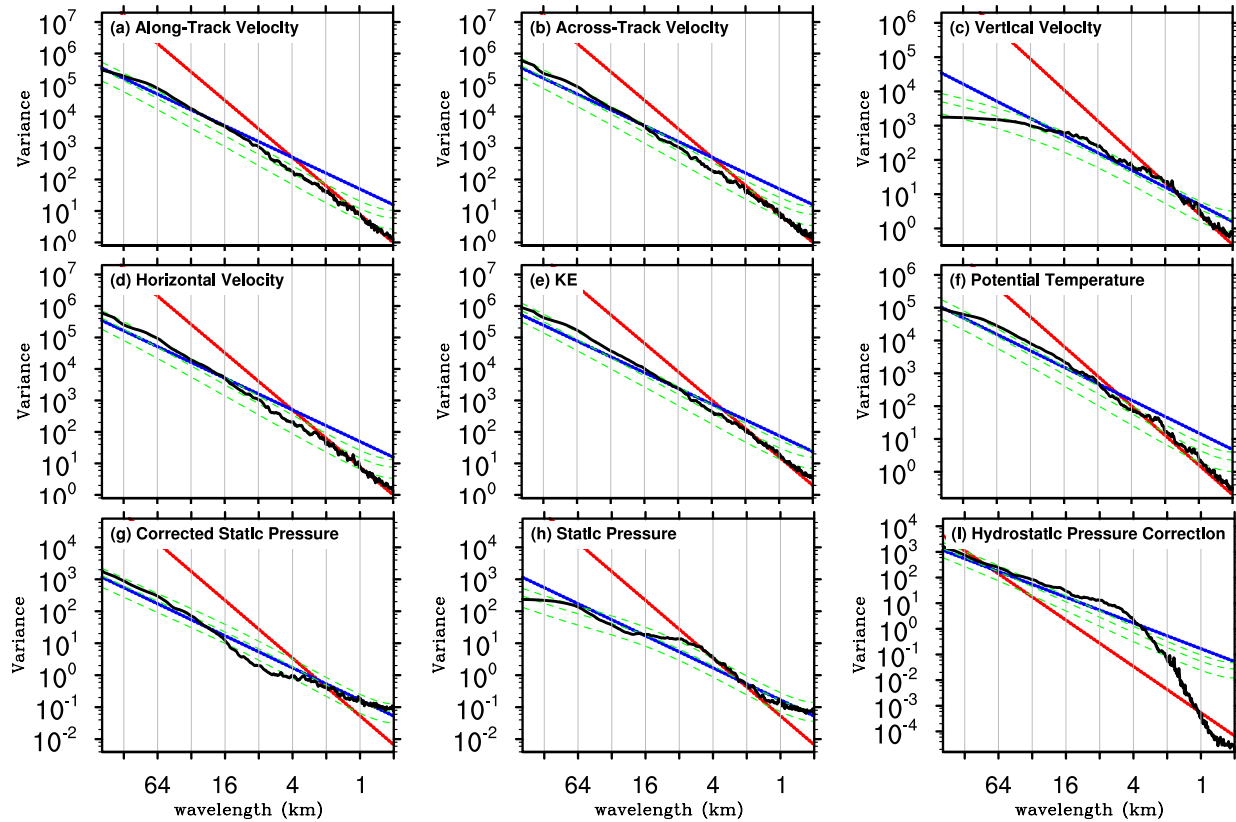
- 139
140 Koch, S. E., Jamison, B. D., Lu, C. G., Smith, T. L., Tollerud, E. I., Girz, C., Wang, N., Lane, T.
141 P., Shapiro, M. A., Parrish, D. D., and Cooper, O. R.: Turbulence and gravity waves within
142 an upper-level front, *J. Atmos. Sci.*, 62, 3885–3908, 2005.
143 Nastrom, G. D., and K. S. Gage, 1985: A Climatology of Atmospheric Wavenumber Spectra of
144 Wind and Temperature Observed by Commercial Aircraft. *J. Atmos. Sci.*, 42, 950–960.
145 Shapiro, M. A., and P. J. Kennedy, 1975: Aircraft Measurements of Wave Motions within
146 Frontal Zone Systems. *Mon. Wea. Rev.*, 103, 1050–1054. doi:
147 [http://dx.doi.org/10.1175/1520-0493\(1975\)103<1050:AMOWMW>2.0.CO;2](http://dx.doi.org/10.1175/1520-0493(1975)103<1050:AMOWMW>2.0.CO;2)
148 Skamarock, W. C., 2004: Evaluating Mesoscale NWP Models Using Kinetic Energy Spectra.
149 *Mon. Wea. Rev.*, 132, 3019–3032.
150



151

152 **Figure R1.01** The spectrum (black line) of GV flight-level aircraft measurement during 5
 153 selected segments (from left to right: J1, J2, J3, M1 and M2) of RF02 in START08: (a) along-
 154 track velocity component (unit: $m^2s^{-2} \cdot m$), (b) across-track velocity component (unit: $m^2s^{-2} \cdot m$
 155), (c) vertical velocity component (unit: $m^2s^{-2} \cdot m$), (d) potential temperature (unit: $K^2 \cdot m$), and
 156 (e) corrected static pressure (unit: $hPa^2 \cdot m$). Green lines show the theoretical Markov spectrum
 157 and the 5% and 95% confidence curves using the lag 1 autocorrelation. The blue (red) reference
 158 lines have slopes of $-5/3$ (-3).

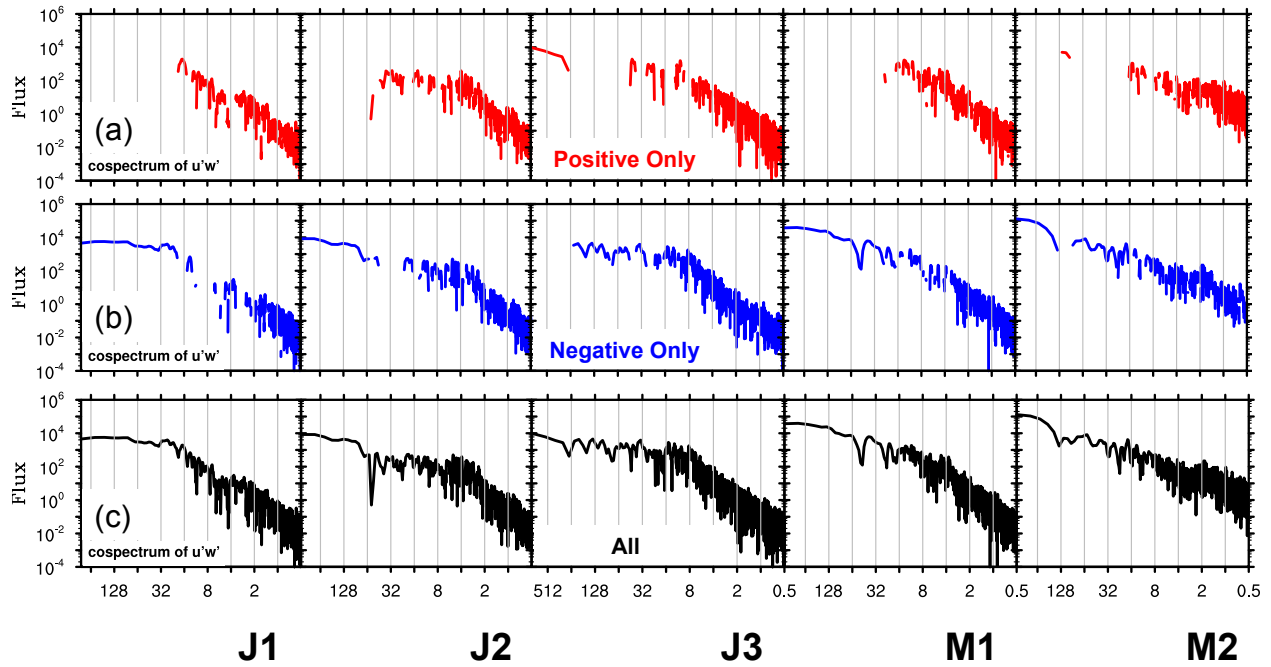
159



160

161 **Figure R1.02** Composite spectrum (black line) of GV flight-level aircraft measurement
 162 averaging over all 68 segments in START08 (colored lines in Fig. 1): (a) along-track velocity
 163 component (unit: $m^2s^{-2} \cdot m$), (b) across-track velocity component (unit: $m^2s^{-2} \cdot m$), (c) vertical
 164 velocity component (unit: $m^2s^{-2} \cdot m$), (d) horizontal velocity component (unit: $m^2s^{-2} \cdot m$), (e)
 165 KE, (f) potential temperature (unit: $K^2 \cdot m$), (g) corrected static pressure (unit: $hPa^2 \cdot m$), (h)
 166 static pressure (unit: $hPa^2 \cdot m$), and (i) hydrostatic pressure correction (unit: $hPa^2 \cdot m$). Green
 167 lines show the composite curves of the theoretical Markov spectrum and the 5% and 95%
 168 confidence curves using the lag 1 autocorrelation. The blue (red) reference lines have slopes of -
 169 $5/3$ (-3). The subplot (e) KE is the sum of (a)-(c).

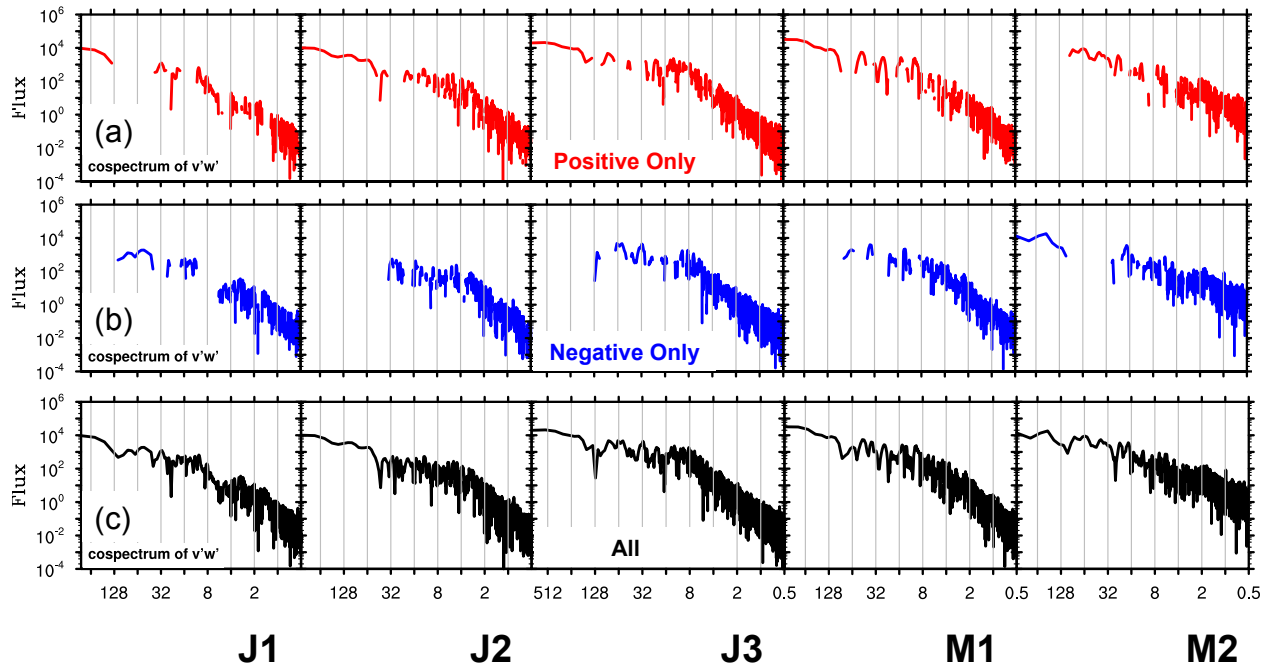
170



171

172 **Figure R1.03** The cospectrum of along-track velocity component u and vertical velocity
 173 component w . (a) The absolute value of the positive only component. (b) The absolute value of
 174 the negative only component. (c) The absolute value of both positive and negative components.

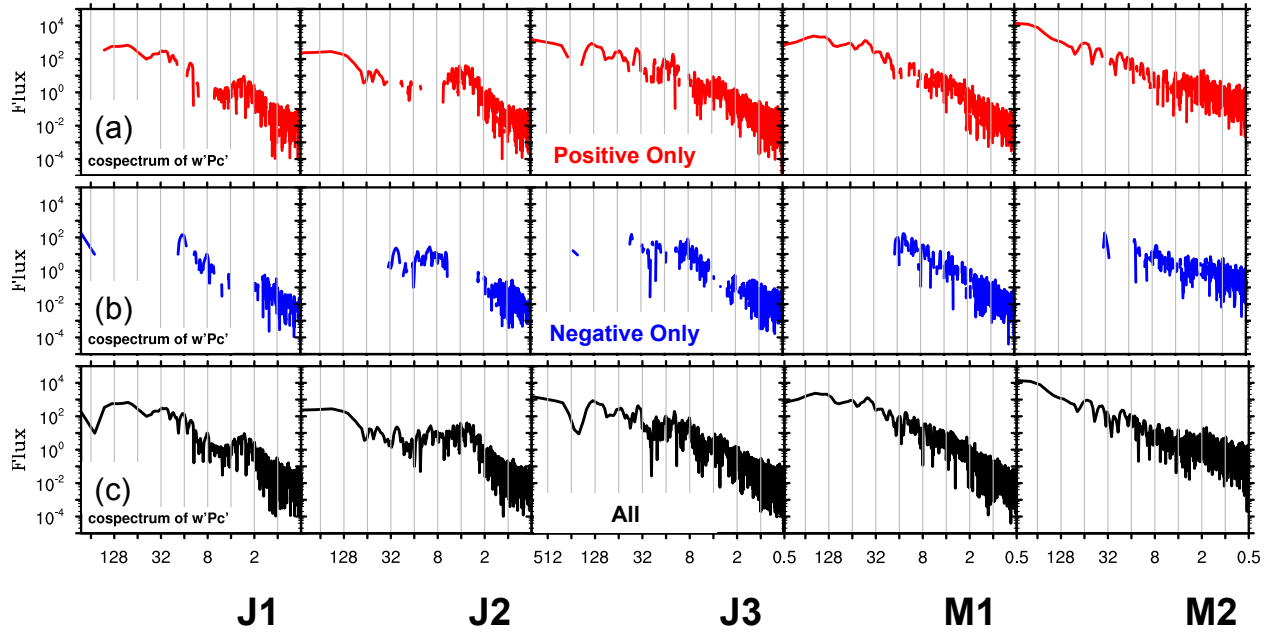
175



176

177 **Figure R1.04** The cosppectrum of across-track velocity component v and vertical velocity
 178 component w . (a) The absolute value of the positive only component. (b) The absolute value of
 179 the negative only component. (c) The absolute value of both positive and negative components.

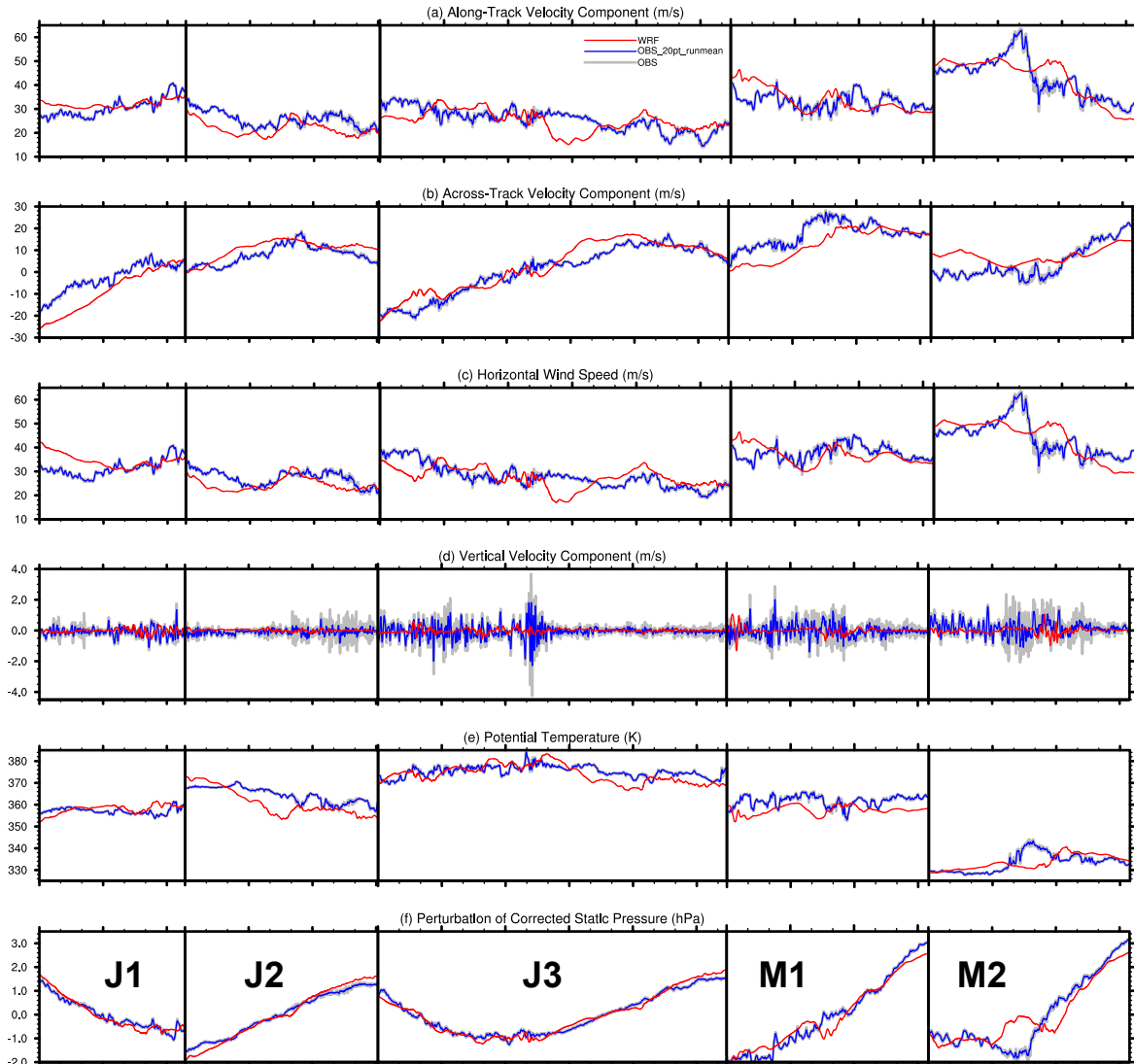
180



181

182 **Figure R1.05** The cospectrum of vertical velocity component w and corrected static pressure
 183 p_c . (a) The absolute value of the positive only component. (b) The absolute value of the negative
 184 only component. (c) The absolute value of both positive and negative components.

185



186
 187 **Figure R1.06** Comparison between GV flight-level aircraft measurements and WRF
 188 simulations during 5 selected segments (from left to right: J1, J2, J3, M1 and M2) of RF02 in
 189 START08: (a) along-track velocity component (m/s), (b) across-track velocity component (m/s),
 190 (c) horizontal wind speed (m/s), (d) vertical velocity component (m/s), (e) potential temperature
 191 (K), and perturbation of corrected static pressure (hPa). The grey lines represent the flight
 192 measurements with 250-m resolution, the blue lines represents 20-point running mean of the grey
 193 lines, and red lines represents the WRF simulations derived from D4 (1.67-km horizontal
 194 resolution) with 10-minute time interval. The series in segment J3 and M2 are reversed to
 195 facilitate the comparison with J1+J2 and M1, respectively. The distance between minor tick
 196 marks in x axis is 100 km. The perturbations in (f) are defined as the differences between the
 197 original data and their mean from their corresponding segments.

Response to Anonymous Referee #2

We thank Anonymous Referee #2 for his/her thorough and insightful comments, which are very helpful in our further revision of the manuscript. We have made every effort to address all the concerns raised. Our point-by-point response is given below.

This manuscript presents an analysis of aircraft measurements of mesoscale gravity waves associated with topography and the upper tropospheric jet region. Fourier and wavelet spectra are investigated, and wavelet cross-correlations are compared to theoretical values for gravity waves. Overall, the results of these comparisons are mixed: some mesoscale features are consistent with gravity waves, but others show inconsistencies that are attributed to measurement errors and flight track fluctuations.

Overall, this is a well written manuscript and a detailed, careful analysis of the START08 data. There are a few issues that the authors gloss over, which I think could be better explored (see below), but generally I have only suggestions for minor revisions.

1. The discussion of spectral slopes from Fig. 4 is superficial and should be better connected to the literature. Reference curves with slopes of -3 and -5/3 are shown, presumably for comparison with the Nastrom-Gage spectrum. But Nastrom & Gage found spectral slopes of -3 only at scales larger than those considered here! The spectra in Fig. 4 are all inside the -5/3 part of the Nastrom-Gage spectrum, so it is not clear why the -3 reference is included. Overall, the $u/v/\theta$ spectra seem to be similar to -5/3 at “larger” scales (256 down to ~16 km), as expected, but are steeper (maybe -3) at smaller scales. It would be interesting to explore the reason for the steepening at small scales. In fact, this small-scale steepening has been noted before (Bacmeister et al., 1996), which should be discussed.

Per this review comment, we will add more discussions of the spectral slopes and make more connections to the literature in the revision. More specifically, there are two main reasons why the -3 power law (red lines in Figure 4 and 5) is included in the current study. First, theoretically speaking, the -3 power law is expected for quasigeostrophic turbulence theory (e.g., Charney, 1971). Second, observationally speaking, the small-scale steepening (slopes of around -3 instead of -5/3) in some cases has been verified in the observational aircraft measurements (e.g., u , v , θ in J1, J2, J3, and M1 as indicated in Figure 4), even though the exact range of the small-scale steepening (slopes of around -3) may be sensitive to the selection of smoothing method or tapering method. It is worth noting that the spectral slope in M2 for u , v , and θ generally follows -5/3 (even at small scales), and that the spectral slope in M1 for u , v , and θ tends to follow -3 at small scales. Even though we are still investigating the physical reason for the above-mentioned slope behavior differences between M1 and M2, one possibility highlighted in the current manuscript is that the differences may be due to the changing background flow (please check the discussion from line 9 in page 4735 to line 2 in 4736).

44 2. Section 5 compares the cross-correlations with gravity wave theory for a few different cases.
45 Discrepancies are found for some cases, especially at small scales, and this is attributed to
46 measurement error or flight track fluctuations. But there seems to be another possible
47 explanation: maybe these fluctuations are just not gravity waves. Could these fluctuations be due
48 to other phenomena, such as shear instabilities, stratified turbulence, etc? This possibility should
49 at least be discussed, and ruled out if possible, if not explored in detail.

50
51

The below sentences will be added around line 4 on page 4746.

52 **“The current study mainly attempts to verify fluctuations with the use of linear**
53 **theory for monochromatic gravity waves. Therefore, in addition to the measurement error,**
54 **the possibilities that those fluctuations may be due to other physical phenomena (e.g.,**
55 **nonlinear dynamics, shear instability and/or turbulence) cannot be completely ruled out.”**

56
57
58

Minor comments:

59 1. Fig. 2 caption: what is the “mesoscale component” of horizontal divergence? Presumably this
60 is just the filtered divergence (not “component”), but how and over what scales?

61
62
63

**As stated in the last sentence of Figure 2 caption, “A band-pass filter is applied to
extract signals with wavelength from 50 to 500km for horizontal divergence.”**

64
65
66
67
68

2. Some figures are too small and difficult to read. For example, Fig. 4, has 25 panels! I had to
zoom 400% to look at this. I suggest breaking this figure into multiple figures, or being more
selective about what to show.

69 **The current manuscript attempts to generalize the characteristics and compare the**
70 **differences among five selected segments in RF02. We believe that it is better to achieve this**
71 **purpose by presenting an ensemble of results in one plot. In revision for Figure 4, we will**
72 **try to make the black lines in front of all the other lines in order to make the plots much**
73 **easier to read.**

74 **Per reviewer's recommendation, and also per suggestion of another reviewer, we**
75 **will revise Figure 4 and Figure 5 using Figure R2.01 and Figure R2.02 given in this**
76 **response below.**

77
78
79
80

3. How are power spectra computed? Are time series windowed (what kind?) or made periodic
in some other way?

81 **The power spectra in Figure 4, including their significant tests, are computed with**
82 **the function provided by the NCAR Command Language (NCL), and the description of the**
83 **function can be found in the below link.**

84 ***http://www.ncl.ucar.edu/Document/Functions/Built-in/specx_anal.shtml***

85 First, the series mean and least squares linear trend are removed (i.e., iopt = 1 in the
86 above function). Second, perform the smoothing by averaging 7 periodogram estimates
87 (i.e., jave=7 in the above function). Third, 10% of the series is tapered (i.e., pct=0.10 in the
88 above function).

89 The below sentences will be added around line 6 on page 4734.

90 “The calculations of the spectra are performed with the “specx_anal” function in
91 the NCAR Command Language (NCL). Several steps are done before the calculations.
92 Firstly, the series mean and least squares linear trend are removed. Secondly, perform the
93 smoothing by averaging 7 periodogram estimates. Thirdly, 10% of the series are tapered.”

94
95 4. In the discussion of the spectral slopes: instead of saying things like “consistent with -5/3”
96 etc, why not actually measure and report the slopes with a least squares fit?
97

98 We thank the reviewer for the suggestion. However, the current manuscript mainly
99 shows that -5/3 and -3 are the representative spectral slopes to be compared with. Yes, one
100 could estimate the slope with a least-squares fit with a running window (e.g., the examples
101 in Figure R2.03 and Figure R2.04 given in this response below), but the estimation will be
102 quite sensitive to the width of the running window and the rather arbitrarily chosen
103 transition wavelength (not shown). We believe showing the reference slopes of -5/3 and -3 is
104 adequate to justify our statement and will not change the final conclusion in the
105 manuscript. Nevertheless, we revise the phrase to be “grossly *consistent with -5/3*” and
106 *alike*.

107

108

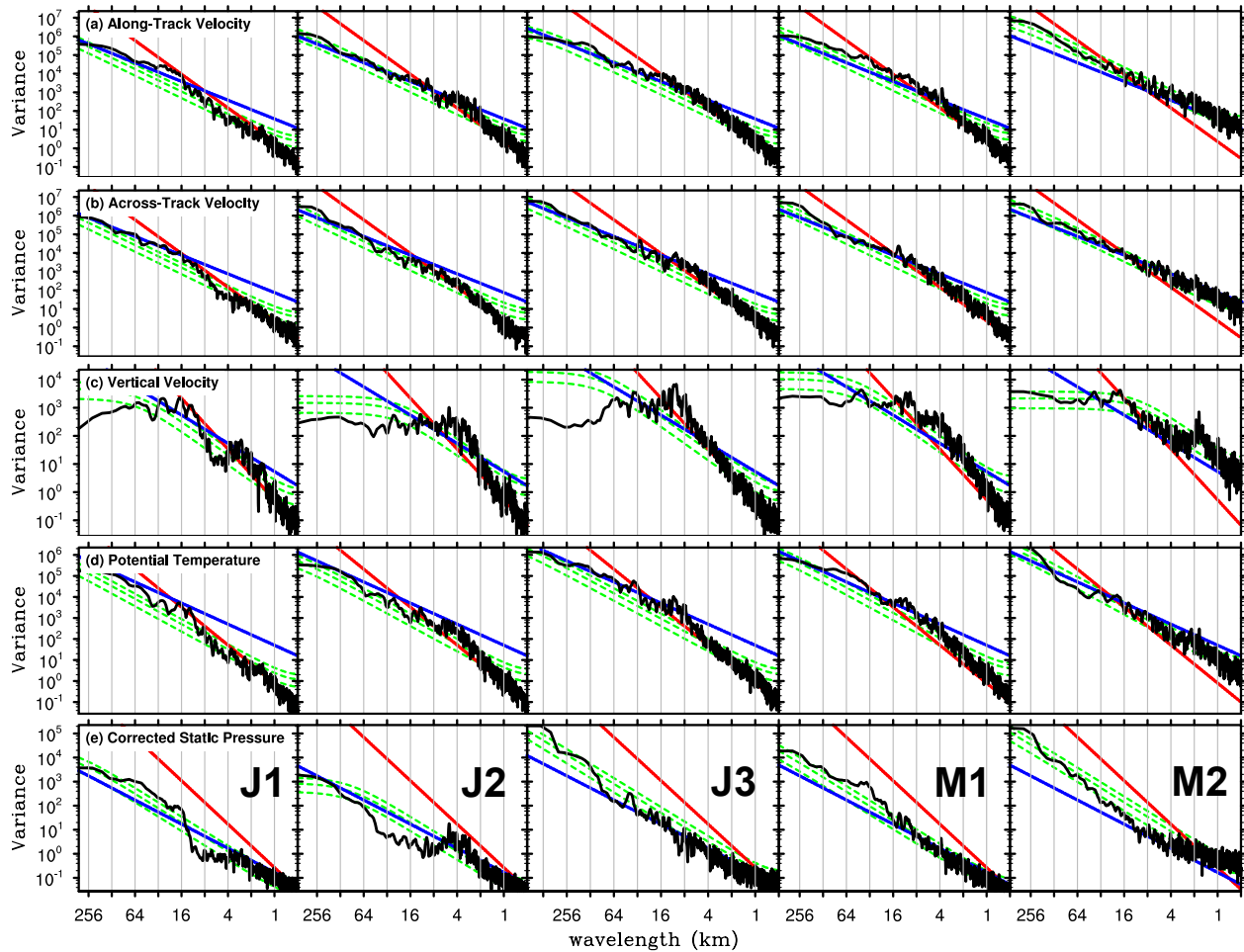
109 **References**

110

111 Charney, J. G.: Geostrophic turbulence, *J. Atmos. Sci.*, 28, 1087–1095, 1971.

112 Nastrom, G. D. and Gage, K. S.: A climatology of atmospheric wavenumber spectra of wind and
113 temperature observed by commercial aircraft, *J. Atmos. Sci.*, 42, 950–960, 1985.

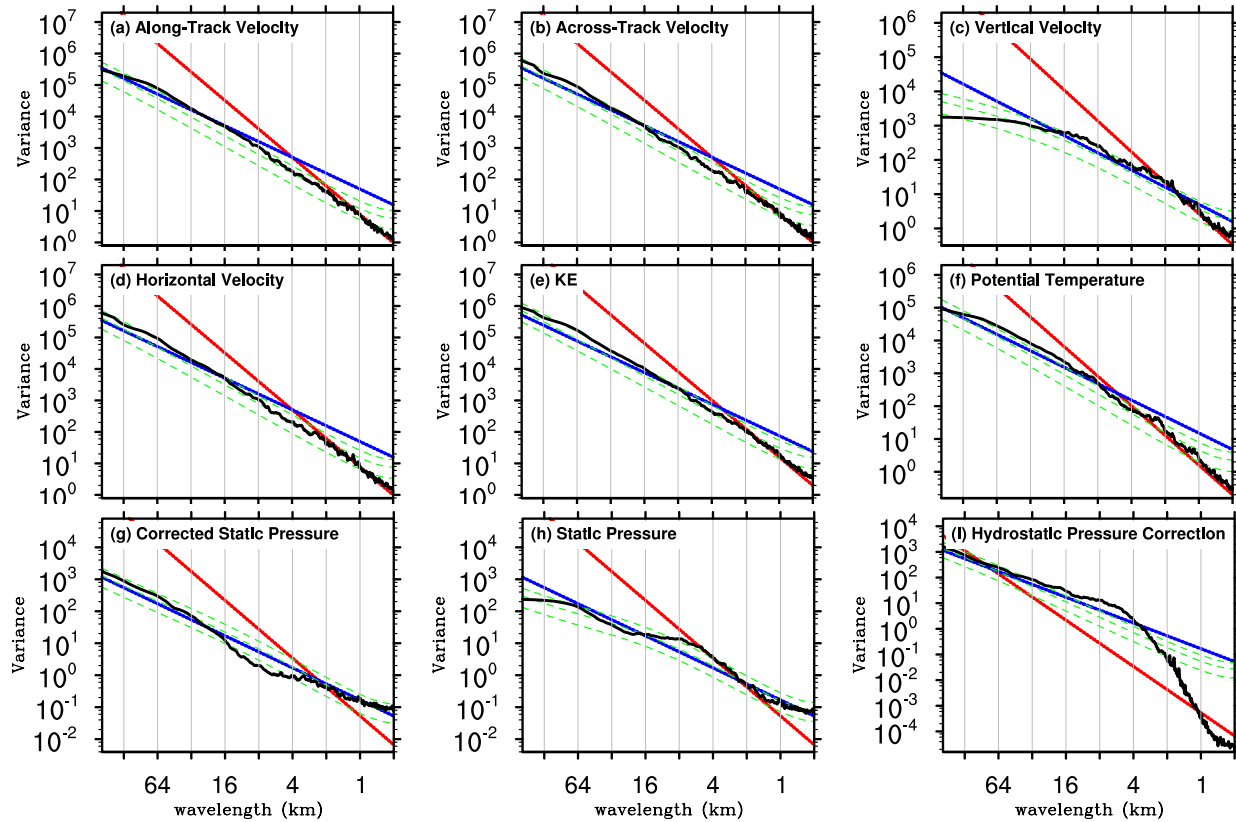
114



115

116 **Figure R2.01** The spectrum (black line) of GV flight-level aircraft measurement during 5
 117 selected segments (from left to right: J1, J2, J3, M1 and M2) of RF02 in START08: (a) along-
 118 track velocity component (unit: $m^2 s^{-2} \cdot m$), (b) across-track velocity component (unit: $m^2 s^{-2} \cdot m$
 119), (c) vertical velocity component (unit: $m^2 s^{-2} \cdot m$), (d) potential temperature (unit: $K^2 \cdot m$), and
 120 (e) corrected static pressure (unit: $hPa^2 \cdot m$). Green lines show the theoretical Markov spectrum
 121 and the 5% and 95% confidence curves using the lag 1 autocorrelation. The blue (red) reference
 122 lines have slopes of $-5/3$ (-3).

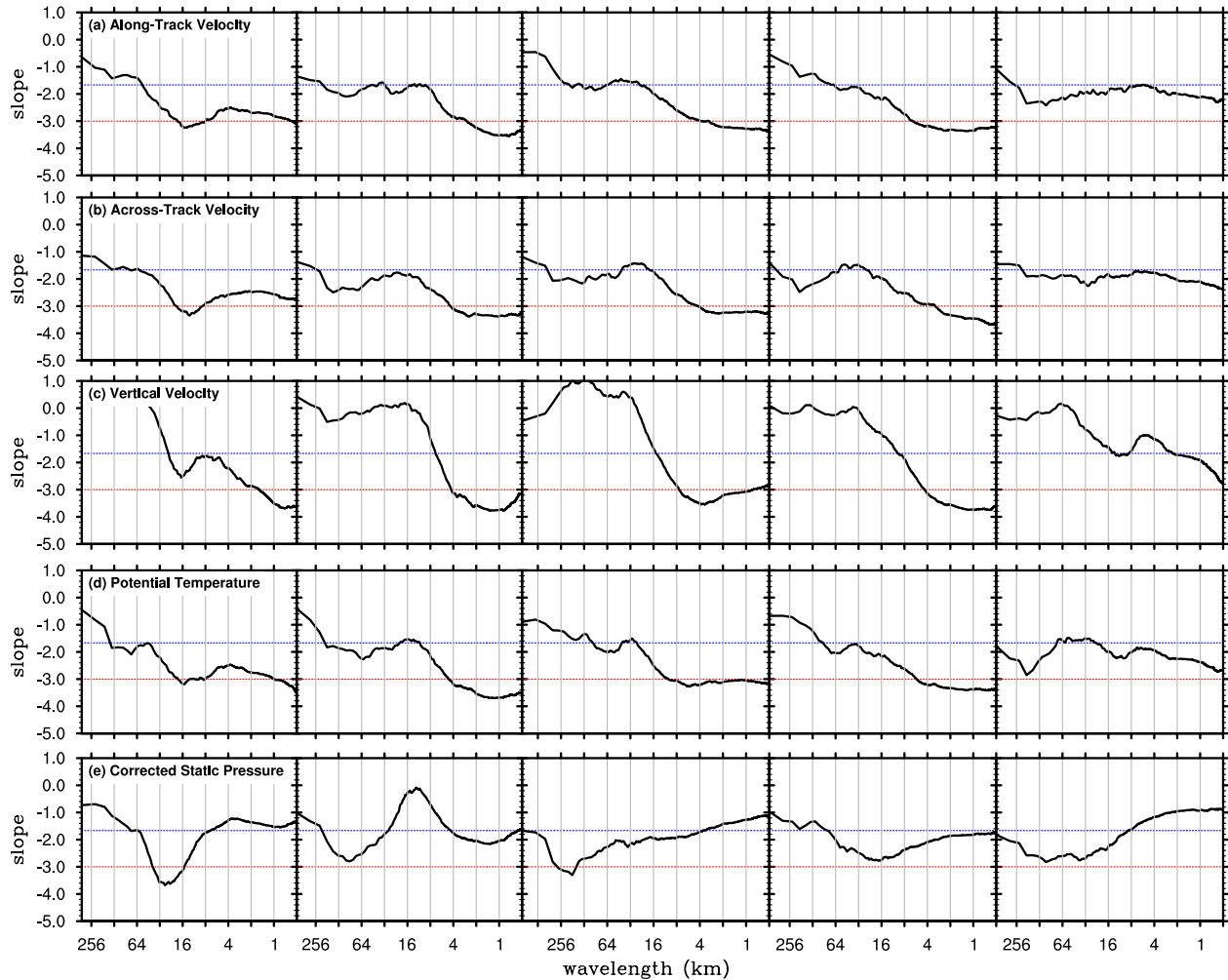
123



124

125 **Figure R2.02** Composite spectrum (black line) of GV flight-level aircraft measurement
 126 averaging over all 68 segments in START08 (colored lines in Fig. 1): (a) along-track velocity
 127 component (unit: $m^2s^{-2} \cdot m$), (b) across-track velocity component (unit: $m^2s^{-2} \cdot m$), (c)
 128 vertical velocity component (unit: $m^2s^{-2} \cdot m$), (d) horizontal velocity component (unit: $m^2s^{-2} \cdot m$), (e)
 129 KE, (f) potential temperature (unit: $K^2 \cdot m$), (g) corrected static pressure (unit: $hPa^2 \cdot m$), (h)
 130 static pressure (unit: $hPa^2 \cdot m$), and (i) hydrostatic pressure correction (unit: $hPa^2 \cdot m$). Green
 131 lines show the composite curves of the theoretical Markov spectrum and the 5% and 95%
 132 confidence curves using the lag 1 autocorrelation. The blue (red) reference lines have slopes of -
 133 $5/3$ (-3). The subplot (e) KE is the sum of (a)-(c).

134



J1

J2

J3

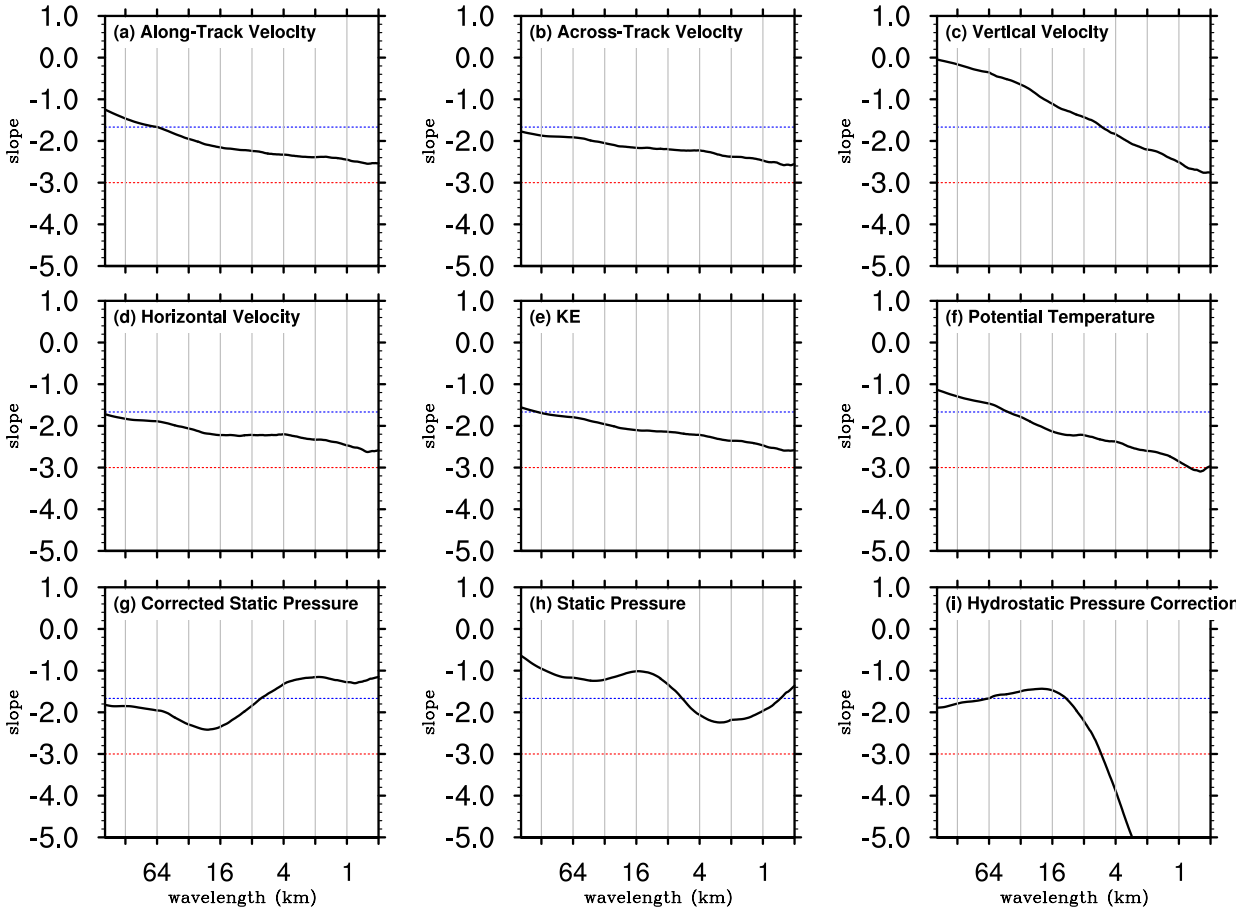
M1

M2

135

136 **Figure R2.03** An example of the spectral slopes based on the results in Figure R2.01. The slopes
 137 are calculated with the linear regression coefficient between the log base 10 of the wavenumber
 138 and the log base 10 of the spectral power. A running window is used over the entire spectrum.
 139 The left boundary of the window is the maximum between wavenumber 1 and one quarter of the
 140 local wavenumber. The right boundary of the window is the minimum between maximum
 141 wavenumber (e.g., half of the total grid points) and four times the local wavenumber.

142



143

144 **Figure R2.04** Same as Figure R2.03, but the calculations are based on the results in Figure

145 R2.02.

146

1 **Response to Anonymous Referee #3**

2 **We thank Anonymous Referee #3 for his/her detailed comments, which are very helpful in**
3 **our further revision of the manuscript. We have made every effort to address all the**
4 **concerns raised. Our point-by-point response is given below.**

5
6 *This is a study of mesoscale gravity waves observed during the START08 field experiment. The*
7 *authors carefully identified gravity waves (GWs) from aircraft measures, and estimated gravity*
8 *wave characteristics using spectral and wavelet analyses. The manuscript shows that spectra of*
9 *horizontal winds and temperature follow the -5/3 power law. Overall, this is a well-constructed*
10 *manuscript. I have a few minor comments. I recommend accept this manuscript after minor*
11 *revision.*

12 *Comments:*

13
14 *1. Line 15, Page 4727: Signals with periods of ~20--60 s. This is mentioned in the abstract and*
15 *conclusion, but I cannot really see how this is estimated in the main text.*

16
17 **“The periods of ~20--60s” in the abstract refers to the sample period, instead of the**
18 **gravity wave period. The typical flight speed is approximately 250 m/s. Therefore, “The**
19 **periods of ~20--60s” in the abstract also corresponds to ~5--15 km.**

20 **In the abstract (around line 16, page 4727), one note will be added as below.**

21 **“...are dominated by signals with periods of around 20–60 s and wavelengths of**
22 **around 5–15 km (assuming that the typical flight speed is approximately 250 m/s). ”**

23 **Similar revision will be made in the conclusion (around line 24, page 4745).**

24
25 *2. Line 1-2, Page 4734: u and θ change drastically near the high terrain (100-200 km west)*
26 *associated with enhanced variance of w. This appears to suggest that this disturbance is*
27 *associated with topography.*

28
29 **The below sentence will be added around line 4 on 4734.**

30 **“The enhanced variances of vertical motion, accompanied by the changes in**
31 **horizontal wind and potential temperature, may be associated with topography for both**
32 **M1 and M2 segments, even though the role of jet cannot be completely ruled out. ”**

33

34 3. 2nd paragraph of Page 4736: *It is remarkable to see a power law can emerge from a very*
35 *limited number of aircraft measurements. It appears to me that the composite spectra horizontal*
36 *velocities (panels a, b, c of Fig. 5) and potential temperature (panel e of Fig. 5) show a slope*
37 *somewhere between -5/3 and -3 for the considered wavenumber range by eye.*

38

39 **Below the scale of ~4~16 km, there appears to be a noticeable departure from -5/3**
40 **for the composite spectra horizontal velocities and potential temperature. However, above**
41 **the scale of ~4~16 km, the above-mentioned spectra generally follow the -5/3 power law.**

42 **The updated version of Figure 5 is shown in Figure R3.01 in this document.**

43

44 4. Line 7 of page 4735: *The logic of this sentence is confusing. Continuity equation is always*
45 *satisfied regardless of the scale of the motion, so it is difficult to use it to explain why power of w*
46 *is much smaller at subsynoptic scale.*

47

48 **Based on the scale analysis of continuity equation, the power of both horizontal**
49 **divergence and vertical motion should be very small at larger scale (e.g., above the order of**
50 **~100 km). Mass may not be conserved if there is strong updraft or downdraft at large scale.**
51 **Therefore, we expect that vertical motion have difficulties in demonstrating much stronger**
52 **power toward larger scale. Similar results can be found in Bei and Zhang (2014) based on**
53 **idealized moist baroclinic waves simulations.**

54

55 5. Line 6 of Page 4742: *rotation could also alter the dispersion relation, hence the phase*
56 *relation between different variables. It is helpful to state clearly what types of GW dispersion*
57 *relationship is used in this study. Is it non-hydrostatic GWs, or inertia-gravity waves?*

58

59 **Earth rotation is considered in the current study. Please check the second**
60 **paragraph (line 6-17) of page 4741. Based on the phase relationship between u and v , we**
61 **have attempted to verify whether the waves in this particular example are influenced by**
62 **earth rotation or not.**

63

64

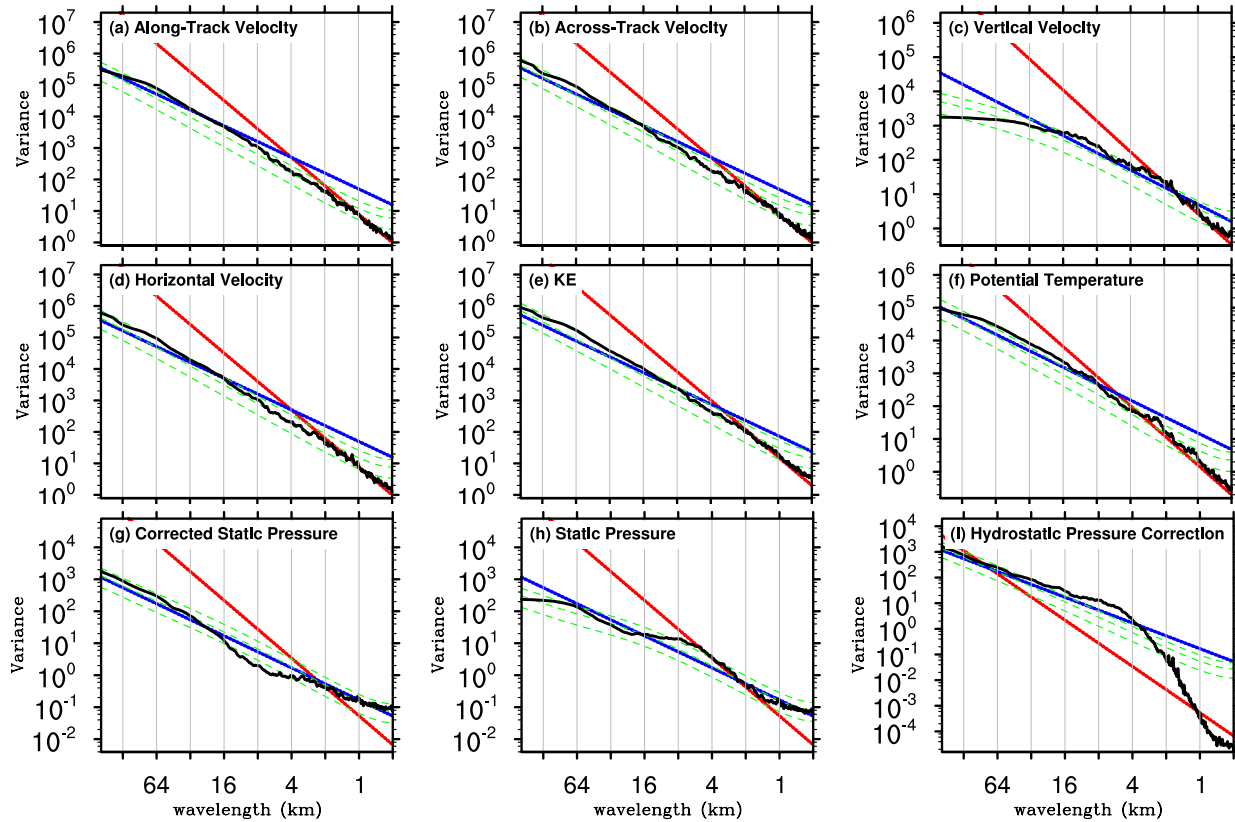
65 **References**

66

67 Bei, N., and F. Zhang, 2014: Mesoscale Predictability of Moist Baroclinic Waves: Variable and
68 Scale Dependent Error Growth. *Advances in Atmospheric Sciences*, 995-1008. doi:

69 10.1007/s00376-014-3191-7.

70



71

72 **Figure R3.01** Composite spectrum (black line) of GV flight-level aircraft measurement
 73 averaging over all 68 segments in START08 (colored lines in Fig. 1): (a) along-track velocity
 74 component (unit: $m^2s^{-2} \cdot m$), (b) across-track velocity component (unit: $m^2s^{-2} \cdot m$), (c)
 75 vertical velocity component (unit: $m^2s^{-2} \cdot m$), (d) horizontal velocity component (unit: $m^2s^{-2} \cdot m$), (e)
 76 KE, (f) potential temperature (unit: $K^2 \cdot m$), (g) corrected static pressure (unit: $hPa^2 \cdot m$), (h)
 77 static pressure (unit: $hPa^2 \cdot m$), and (i) hydrostatic pressure correction (unit: $hPa^2 \cdot m$). Green
 78 lines show the composite curves of the theoretical Markov spectrum and the 5% and 95%
 79 confidence curves using the lag 1 autocorrelation. The blue (red) reference lines have slopes of -
 80 $5/3$ (-3). The subplot (e) KE is the sum of (a)-(c).

81

Response to Anonymous Referee #4

We thank Anonymous Referee #4 for his/her thorough and insightful comments, which are very helpful in our further revision of the manuscript. We have made every effort to address all the concerns raised. Our point-by-point response is given below.

The paper describes aircraft measurements that have been collected in the upper troposphere and lower stratosphere over the continental United States, and analyzes the gravity waves present in these measurements. One research flight of the START08 campaign was dedicated to gravity waves in the Upper Troposphere and Lower Stratosphere. This is, a priori, the first aircraft research flight dedicated to this theme. It is of interest to describe and document it. The paper shows: - that multiple events of gravity waves occurred along the flight track, - both orographic and non-orographic waves are captured, - the analysis using wavelets allows to identify wave packets, but there are difficulties; part of the high frequency signal corresponds to measurement noise.

Overall, the paper leaves the impression that the analysis, even with a wealth of high-resolution measurements, is difficult. Although much analysis is discussed with care, the paper leaves the reader somewhat unsatisfied. The description of the flights and the results of the spectral analysis of the measurements are valuable and of interest. Perhaps the paper in its present form contains too much information, in particular in the figures, and the reader may have difficulty in clearly singling out essential messages. I recommend publication after some revision to improve the focus of the study.

Major points

1. Many of the figures are difficult to read because they cover too much information. As an example, figure 4 contains 25 panels, each containing 6 curves... This needs to be reduced if information is to be retained from this figure. For instance, is it necessary to distinguish along and across-track spectra? They seem very similar, and unless one fears that the measurements are introducing a bias, I do not see any physical reason not to combine these into a wind speed and plot spectra for the wind speed. Whereas spectra of u_h , w , and potential temperature are common, I do not know of expectations for the spectra of static pressure. I believe one could do without this row of plots. Finally, do all the five legs of the flight really need to be plotted separately, or could some be combined or omitted?

Similarly: - figure 2 could contain less maps (e.g. 1800, 1950, 2210 and 0020UTC) - figure 5 could contain less panels (e.g. c, d, e) - figures 6 and 7 could contain less panels (e.g. horizontal velocity, w , θ for figure 6) - in each of the four figures 8, 9, 10 and 11: several curves are repeated many times, to display phase relationships (e.g. w is plotted 6 times among 9 panels!). This is excessive, there are other ways to present such information (e.g. profiles in a single plot, displaced in the vertical so as not to overlap, and with vertical lines indicating extrema (or zeros) of one reference signal...

45 The current manuscript attempts to generalize the characteristics and compare the
46 differences among five selected segments in RF02. We believe that it is better to achieve this
47 purpose by presenting an ensemble of results in one plot. In revision for Figure 4, we will
48 try to make the black lines in front of all the other lines in order to make the plots much
49 easier to read.

50 The updated Figure 4 and Figure 5 are presented as Figure R4.01 and Figure R4.02
51 in the current document.

52 In one of the earlier version of the manuscript for Zhang et al. (2015), we have tried
53 to plot all the variables into one plot for Figure 8-10. Even though the results look readable
54 for mesoscale examples, the plots actually look very messy for the short-scale examples.
55 This is one of the reasons why we attempt to verify the phase relationship one by one, and
56 to investigate the propagating characteristics from different aspects in each subplot for
57 Figure 8-10.

58
59 *2. While the figures provide too much information, it is sometimes difficult to find certain*
60 *quantitative informations on the gravity waves. For example on p4733, line 27 onward: what are*
61 *the largest amplitudes mentionned in the text? p4745: line 18: similarly, what are the*
62 *amplitudes?*

63
64 The below note will be added around line 28 on page 4733.

65 “The largest amplitude of w (magnitude of above 2 m/s) is during the middle
66 portion of segment J3 (location 680-780 km) on the lee slopes of the Rocky Mountains (also
67 see the discussion in section 5.2 on Figure 11).”

68 The below note will be added around line 19 on page 4745.

69 “...it is found that there are clear signals of significant mesoscale variations with
70 wavelengths ranging from 50 to 500 km in almost every segment of the 8 h flight (order
71 ranging from 0.01 m/s to 1.0 m/s in vertical motion), which took place mostly in the lower
72 stratosphere.”

73
74 *3. WRF simulations are used in Figure 2 to exhibit the flow configuration, but the comparison*
75 *between the simulated GW and the observed ones is hardly discussed.*

76
77 Figure R4.03 in this document demonstrates the comparison between aircraft
78 measurements and high-resolution WRF simulations. Preliminary analysis shows that
79 WRF successfully captures the variations in wind, potential temperature, and pressure,
80 especially for segment J1, J2, J3, and M1. Probably due to upscale error growth with
81 relatively long-time integration for segment M2, there is indeed a ~150-km distance
82 between the observed V maximum location (at location ~400 km in M2) and the simulated
83 one (at location ~550 km in M2). Also, the observed V maximum is larger than the
84 simulated one (~60 m/s versus ~50 m/s). With that being said, the forecast error is within a
85 reasonable range, and the aircraft did manage to obtain the data within the jet exit region.

86 **However, it is beyond to the scope of the current study to investigate the**
87 **consistencies and differences between aircraft measurements and WRF. WRF simulations**
88 **and dynamics of the gravity waves will be examined in a separate study. In particular,**
89 **based on the high-resolution simulations, we will investigate the sensitivity of wave**
90 **response to the mean flow speed, wind direction, wind shear, and altitude, as suggested in**
91 **the above comments.**

92

93

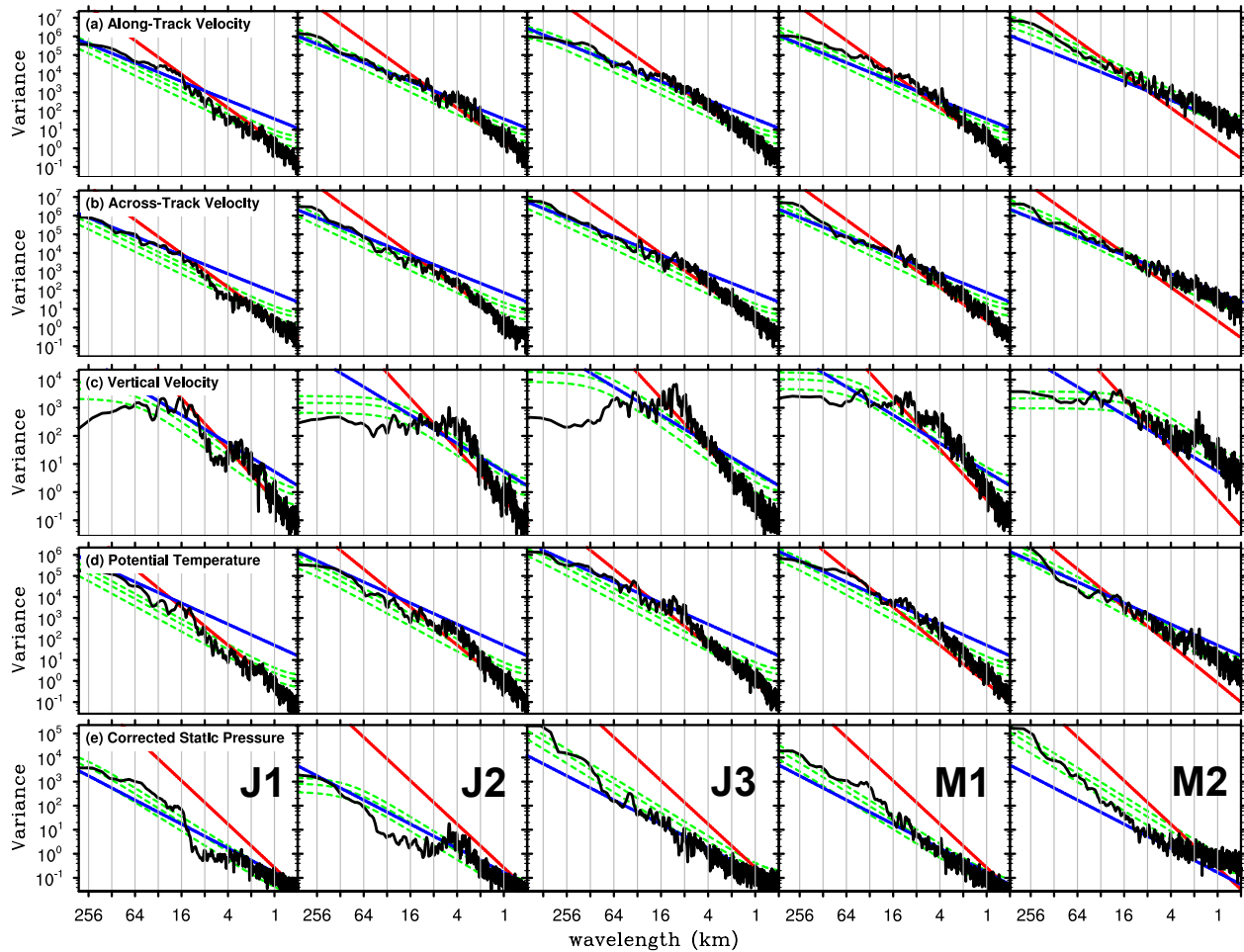
94 **References**

95

96 Zhang, F., J. Wei, M. Zhang, K.B. Bowman, L.L. Pan, E. Atlas, and S.C. Wofsy, 2015: Aircraft
97 measurements of gravity waves in the upper troposphere and lower stratosphere during the
98 START08 Field Experiment, *Atmos. Chem. Phys. Discuss.*, 15, 4725-4766,
99 doi:10.5194/acpd-15-4725-2015.

100

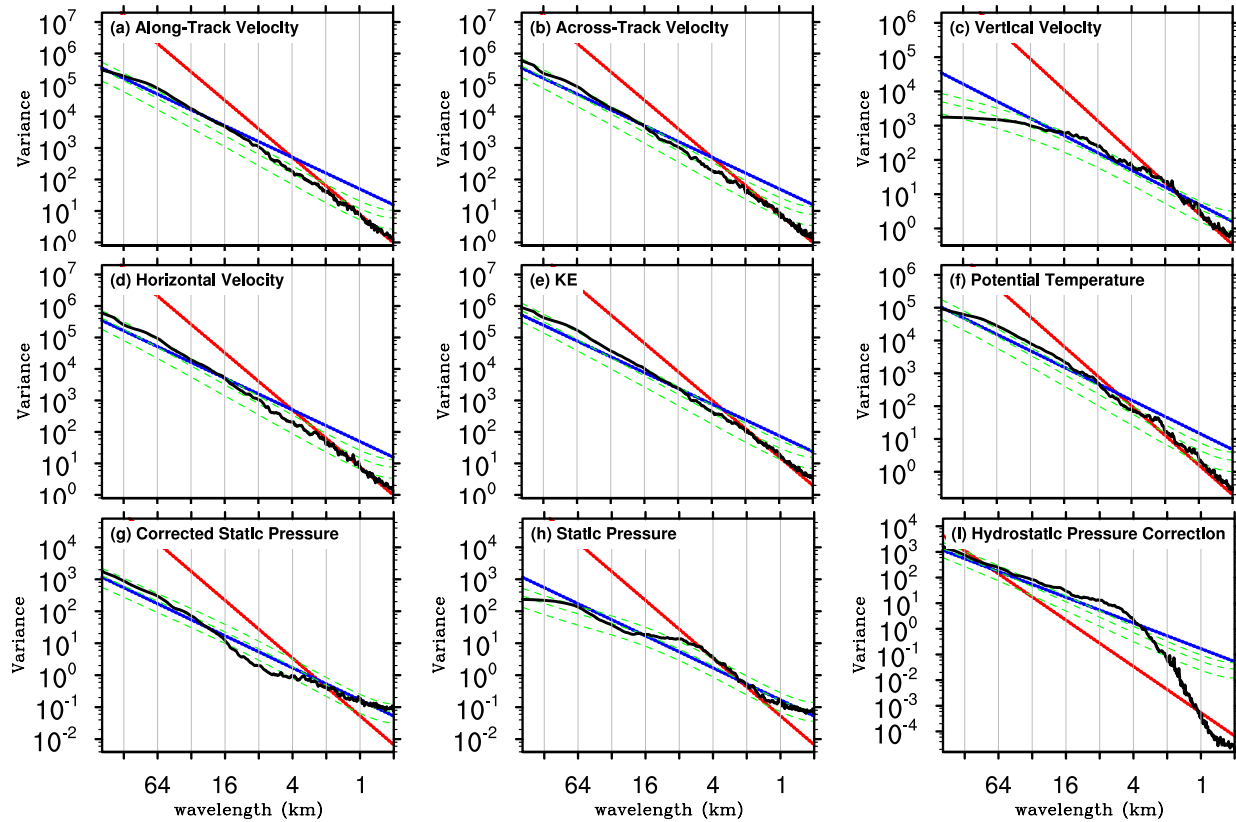
101



102

103 **Figure R4.01** The spectrum (black line) of GV flight-level aircraft measurement during 5
 104 selected segments (from left to right: J1, J2, J3, M1 and M2) of RF02 in START08: (a) along-
 105 track velocity component (unit: $m^2 s^{-2} \cdot m$), (b) across-track velocity component (unit: $m^2 s^{-2} \cdot m$
 106), (c) vertical velocity component (unit: $m^2 s^{-2} \cdot m$), (d) potential temperature (unit: $K^2 \cdot m$), and
 107 (e) corrected static pressure (unit: $hPa^2 \cdot m$). Green lines show the theoretical Markov spectrum
 108 and the 5% and 95% confidence curves using the lag 1 autocorrelation. The blue (red) reference
 109 lines have slopes of $-5/3$ (-3).

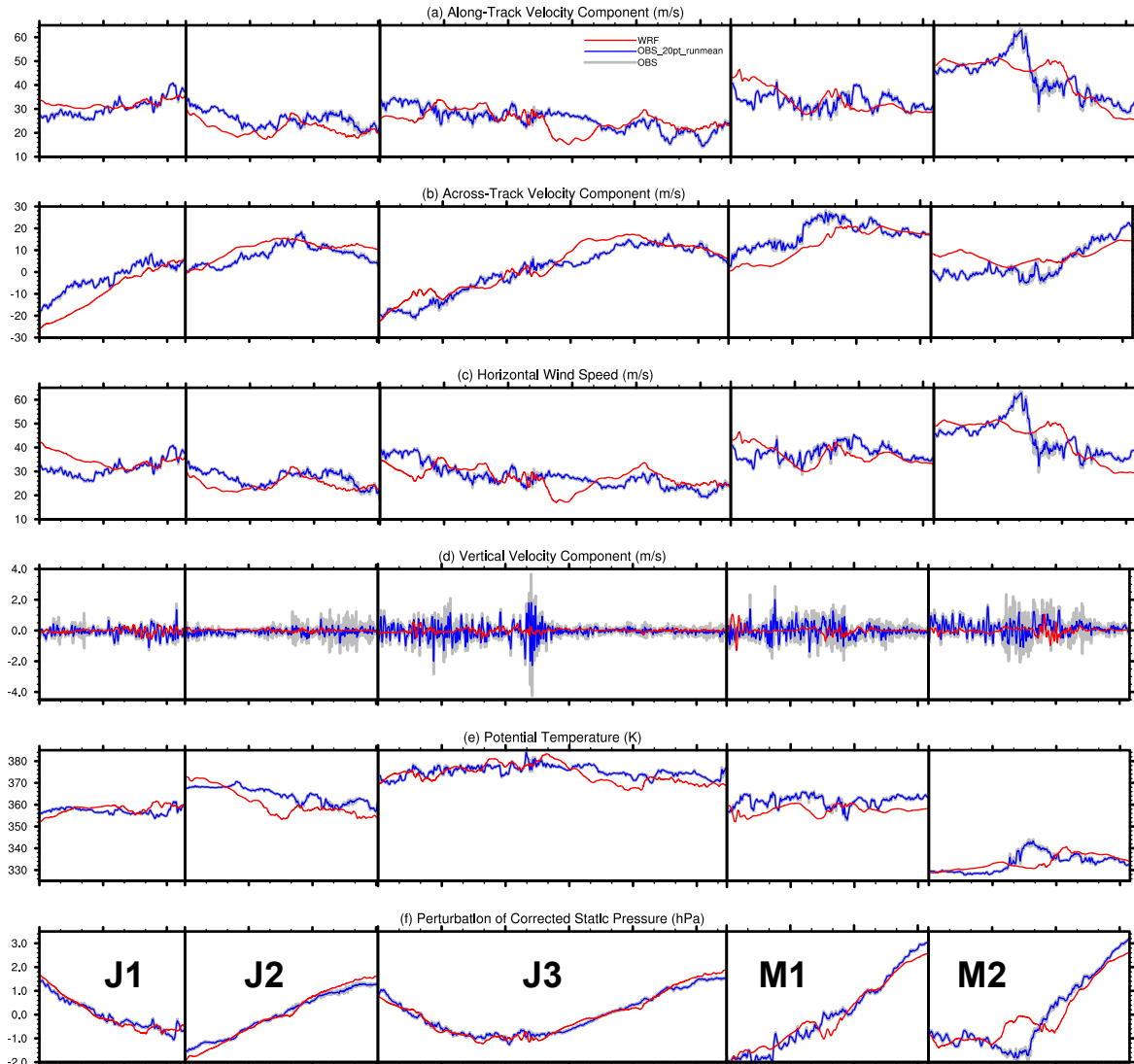
110



111

112 **Figure R4.02** Composite spectrum (black line) of GV flight-level aircraft measurement
 113 averaging over all 68 segments in START08 (colored lines in Fig. 1): (a) along-track velocity
 114 component (unit: $m^2s^{-2} \cdot m$), (b) across-track velocity component (unit: $m^2s^{-2} \cdot m$), (c)
 115 vertical velocity component (unit: $m^2s^{-2} \cdot m$), (d) horizontal velocity component (unit: $m^2s^{-2} \cdot m$), (e)
 116 KE, (f) potential temperature (unit: $K^2 \cdot m$), (g) corrected static pressure (unit: $hPa^2 \cdot m$), (h)
 117 static pressure (unit: $hPa^2 \cdot m$), and (i) hydrostatic pressure correction (unit: $hPa^2 \cdot m$). Green
 118 lines show the composite curves of the theoretical Markov spectrum and the 5% and 95%
 119 confidence curves using the lag 1 autocorrelation. The blue (red) reference lines have slopes of -
 120 $5/3$ (-3). The subplot (e) KE is the sum of (a)-(c).

121



122
 123 **Figure R4.03** Comparison between GV flight-level aircraft measurements and WRF
 124 simulations during 5 selected segments (from left to right: J1, J2, J3, M1 and M2) of RF02 in
 125 START08: (a) along-track velocity component (m/s), (b) across-track velocity component (m/s),
 126 (c) horizontal wind speed (m/s), (d) vertical velocity component (m/s), (e) potential temperature
 127 (K), and perturbation of corrected static pressure (hPa). The grey lines represent the flight
 128 measurements with 250-m resolution, the blue lines represents 20-point running mean of the grey
 129 lines, and red lines represents the WRF simulations derived from D4 (1.67-km horizontal
 130 resolution) with 10-minute time interval. The series in segment J3 and M2 are reversed to
 131 facilitate the comparison with J1+J2 and M1, respectively. The distance between minor tick
 132 marks in x axis is 100 km. The perturbations in (f) are defined as the differences between the
 133 original data and their mean from their corresponding segments.

1 **Aircraft Measurements of Gravity Waves in the Upper Troposphere and Lower**
2 **Stratosphere during the START08 Field Experiment**

3
4 Fuqing Zhang^{1*}, Junhong Wei¹, Meng Zhang¹, Kenneth P. Bowman², Laura L. Pan³, Elliot
5 Atlas⁴, and Steve C. Wofsy⁵

- 6
7 1. Department of Meteorology, The Pennsylvania State University, University Park,
8 Pennsylvania
9 2. Department of Atmospheric Sciences, Texas A&M University, College Station, Texas
10 3. National Center for Atmospheric Research, Boulder, Colorado
11 4. Rosenstiel School of Marine and Atmospheric Science, University of Miami, Miami,
12 Florida
13 5. Division of Engineering and Applied Science/Department of Earth and Planetary
14 Science, Harvard University, Cambridge, Massachusetts

15
16
17 **Submitted to *Atmospheric Chemistry and Physics* for publication**

18 **Revised submission, 25 April 2015**

Fuqing Zhang 4/25/2015 9:52 AM
Deleted: Initial Submission, 3 November 2014
Fuqing Zhang 4/25/2015 9:52 AM
Deleted: 28 December 2014

19
20
21

Corresponding author address: Professor Fuqing Zhang, Dept. of Meteorology, The Pennsylvania State University, University Park, PA 16802. E-mail: fzhang@psu.edu

25
26
27
28
29
30
31
32
33
34
35
36
37
38
39
40
41
42
43
44
45
46

Abstract

This study analyzes *in-situ* airborne measurements from the 2008 Stratosphere-Troposphere Analyses of Regional Transport (START08) experiment to characterize gravity waves in the extratropical upper troposphere and lower stratosphere (ExUTLS) region. The focus is on the second research flight (RF02), which took place on 21-22 April 2008. This was the first airborne mission dedicated to probing gravity waves associated with strong upper-tropospheric jet-front systems. Based on spectral and wavelet analyses of the *in-situ* observations, along with a diagnosis of the polarization relationships, clear signals of mesoscale variations with wavelengths ~50-500 km are found in almost every segment of the 8-hr flight, which took place mostly in the lower stratosphere. The aircraft sampled a wide range of background conditions including the region near the jet core, the jet exit and over the Rocky Mountains. In contrast to the long wavelength mesoscale variations, smaller-scale wavelike oscillations below 50 km are found to be quite transient. In particular, aircraft measurements of several flight segments are dominated by signals with sampled periods of ~20~60 seconds and wavelengths of ~5~15 km, (assuming that the typical flight speed is approximately 250 m/s). We speculate that at least part of these nearly-periodic high-frequency signals are a result of intrinsic observational errors in the aircraft measurements or small-scale flight-altitude fluctuations that are difficult to fully characterize. Despite the presence of possibly spurious wave oscillations in several flight segments, the power spectra of horizontal winds and temperature averaged over the analyzed START08 flight segments generally follow the $-5/3$ power law.

Fuqing Zhang 4/25/2015 9:52 AM
Deleted: .

Fuqing Zhang 4/25/2015 9:52 AM
Deleted: closely

49 **1. Introduction**

50 One of the challenges to understanding the extratropical upper troposphere and lower
51 stratosphere (ExUTLS) is that dynamical processes with a wide range of scales occur in the
52 region. Gravity waves, in particular, are known to play a significant role in determining the
53 structure and composition of the ExUTLS. Tropopause jets and fronts are significant sources of
54 gravity waves (O’Sullivan and Dunkerton 1995; Reeder and Griffins 1996; Zhang 2004; Wang
55 and Zhang 2007; Mirzaei et al. 2014; Wei and Zhang 2014, 2015), along with surface
56 topography (Smith 1980) and moist convection (Lane et al. 2001). Gravity waves above the jet
57 may be responsible for double or multiple tropopauses (Yamanaka et al. 1996; Pavelin et al.
58 2001) and may contribute to layered ozone or PV structures (Bertin et al. 2001). Also, strong
59 horizontal and vertical shear in the layer and the discontinuity in static stability at the tropopause
60 provide a favorable environment to reflect, capture, break and dissipate gravity waves generated
61 in the lower troposphere, such as those produced by surface fronts (Plougonven and Snyder
62 2007). Gravity wave breaking and wave-induced turbulence (e.g., Koch et al. 2005) can
63 contribute significantly to mixing of trace gases in the ExUTLS, thereby affecting chemical
64 composition (Vaughan and Worthington, 2000). Also, convectively-generated gravity waves
65 may extend the impact of moist convection far above cloud tops through wave-induced mixing
66 and transport (Lane et al. 2004).

67 In particular, mesoscale gravity waves with horizontal wavelength of ~50~500 km are
68 known to occur in the vicinity of unbalanced upper-tropospheric jet streaks and on the cold-air
69 side of surface frontal boundaries (Uccellini and Koch 1987; Plougonven and Zhang 2014). This
70 phenomenon has been identified repeatedly in both observational studies (Uccellini and Koch
71 1987; Schneider 1990; Fritts and Nastrom 1992; Ramamurthy et al. 1993; Bosart et al. 1998;

72 Koppel et al. 2000; Rauber et al. 2001; Plougonven et al. 2003) and numerical investigations of
73 the observed cases (Powers and Reed 1993; Pokrandt et al. 1996; Kaplan et al. 1997; Zhang and
74 Koch 2000; Zhang et al. 2001, 2003; Koch et al. 2001, 2005; Lane et al. 2004). In addition,
75 idealized simulations of dry baroclinic jet-front systems in a high-resolution mesoscale model
76 have been performed to investigate the generation of mesoscale gravity waves (Zhang 2004), the
77 sensitivity of mesoscale gravity waves to the baroclinicity of jet-front systems (Wang and Zhang
78 2007), and the source of gravity waves with multiple horizontal scales (Lin and Zhang 2008).
79 Most recently, Wei and Zhang (2014, 2015) studied the characteristics and potential source
80 mechanisms of mesoscale gravity waves in moist baroclinic jet-front systems with varying
81 degree of convective instability.

82 Advances in space technology provide the means to observe gravity waves in detail.
83 Recent studies have demonstrated that satellites such as Microwave Limb Sounder (MLS) and
84 Advanced Microwave Sounding Unit-A (AMSU-A) offer quantitative information of gravity
85 waves in the middle atmosphere (Alexander and Rosenlof 2003; Wu and Zhang 2004; Zhang et
86 al. 2013). In addition to satellite measurements, gravity waves are also observed by surface
87 observations (Einaudi et al. 1989; Grivet-Talocia et al. 1999; Koppel et al. 2000), high-resolution
88 radionsonde networks (Vincent and Alexander 2000; Wang and Geller 2003; Zhang and Yi
89 2007; Gong and Geller 2010), radars (Vaughan and Worthington 2000, 2007), and super-
90 pressure balloons (Hertzog and Vial 2001).

91 Among the abovementioned observational tools, aircraft have also been widely used as
92 *in-situ* measurements of gravity waves. Probably since Radok (1954), which was one of the first
93 observations of mountain waves with aircraft, past aircraft field campaigns have mainly focused
94 on terrain-induced gravity waves (Radok 1954; Vergeiner and Lilly 1970; Lilly and Kennedy

95 1973; Smith 1976; Karacostas and Marwitz 1980; Brown 1983; Moustauoui et al. 1999;
96 Leutbecher and Volkert 2000; Poulos et al. 2002; Dornbrack et al. 2002; Doyle et al. 2002;
97 Smith et al. 2008). The recent Terrain-Induced Rotor Experiment (T-REX) in March-April 2006
98 (Grubišić et al. 2008) was the first full research project to use the National Science Foundation
99 (NSF) – National Center for Atmospheric Research (NCAR) Gulfstream V (GV) (Laursen et al.
100 2006), which has better Global Positioning System (GPS) accuracy than the previous versions.
101 The National Aeronautics and Space Administration (NASA) high-altitude ER-2 research
102 aircraft was also employed during the recent Cirrus Regional Study of Tropical Anvils and
103 Cirrus Layers Florida Area Cirrus Experiment (CRYSTAL-FACE) (Jensen et al. 2004), which
104 conducted research flights in the vicinity of sub-tropical and tropical deep convection to study
105 the effects of convectively generated gravity waves (Wang et al. 2006). However, systematic *in-*
106 *situ* measurements of mesoscale gravity waves, especially those associated with upper-
107 tropospheric jet-front systems in the ExUTLS are very scarce. Relevant work includes Nastrom
108 and Fritts (1992) and Fritts and Nastrom (1992), who used commercial aircraft measurements to
109 infer the different sources of gravity waves (convections, front, topography, and jet streaks).
110 They found that mesoscale variances of horizontal wind and temperature were large at the jet-
111 front vicinity regions. However, little is known quantitatively about the generation mechanisms,
112 propagation and characteristics of gravity waves associated with the tropospheric jet streaks.
113 This is due in part to the fact that gravity waves are transient in nature and hard to resolve with
114 regular observing networks (Zhang et al. 2004).

115 The recent Stratosphere-Troposphere Analyses of Regional Transport 2008 (START08)
116 experiment was conducted to examine the chemical structure of the ExUTLS in relation to
117 dynamical processes spanning a range of scales (Pan et al. 2010). In particular, one specific goal

118 of START08 was to observe the properties of gravity waves generated by multiple sources,
119 including jets, fronts, and topography. During the START08 field campaign, a total of 18
120 research flight (RF) missions were carried out during April-June 2008 from the NCAR aviation
121 facility in Broomfield, Colorado (also see the online field catalog of the 18 RFs at
122 http://catalog.eol.ucar.edu/start_08/missions/missions.html). The second flight (RF02), which
123 occurred on 21-22 April 2008, was dedicated, to our knowledge for the first time, to probing
124 mesoscale gravity waves associated with a strong upper-tropospheric jet-front system, even
125 though some previous studies may have recognized the presence of these waves (e.g., Shapiro
126 and Kennedy 1975; Koch et al. 2005). Although only one flight specifically targeted gravity
127 waves, many of the other flights during START08 obtained high-quality observations of gravity
128 waves in the ExUTLS under a wide range of meteorological conditions. This study is an analysis
129 of the gravity wave observations from the START08 mission.

130 A brief description of the experimental design for RF02 and its corresponding
131 meososcale simulation are presented in section 2, followed in section 3 by a review of the flight-
132 level measurements. Section 4 investigates the localized wave variance with wavelet analysis
133 and examines the polarization relationship based on cospectrum/quadrasmuspectrum analysis.
134 Several examples of wave-like variances are shown and discussed in section 5. Section 6
135 contains a summary.

136

137 2. Experimental design

138 The GV research aircraft is ideally suited for investigating gravity waves in the ExUTLS
139 region. The flight ceiling of the aircraft is about 14 km with the START08 payload, which
140 enables sampling the vertical structure of the ExUTLS. With a typical flight speed of ~250 m/s at

Fuqing Zhang 4/25/2015 9:52 AM

Deleted: .

142 cruise altitude, the flight duration of ~8 hours for a single flight enables the GV to sample a large
143 geographic area with high-resolution (1-Hz) *in-situ* observations. A total of 68 flight segments
144 (color lines in Fig. 1) during the START08 are selected for analysis (also see Fig. 2 in Pan et al.
145 2010 for GV ground tracks of the 18 RFs). Each of these flight segments is longer than 200 km
146 and has near-constant flight-level static pressure and a relatively straight path. This will largely
147 eliminate spurious wave variance due to rapid changes in direction or altitude. In particular, the
148 RF02 mission was conducted over the central United States (38.87-51.10°N, 94.00-109.95°W) to
149 study the gravity wave excitation from a jet-front system and topography in the ExUTLS (Fig. 2
150 and Table 1). It started at 17:53 UTC on 21 April 2008 and finished at 02:54 UTC on 22 April
151 2008. This ~8-hour flight covered a total horizontal distance of ~6700 km, mostly in the lower
152 stratosphere. Five flight segments (thick blue lines in Fig. 1; thick blue lines in Fig. 2b-Fig. 2f;
153 details in section 3) in RF02 are used here. For most of the 5 flight segments, the aircraft flew at
154 an altitude of ~12.5 km (red lines in Fig. 3d; Table 1) and at a speed of ~250 ms⁻¹ (Table 1).

155 The Weather Research and Forecast (WRF) model (Skamarock et al. 2005) was used for
156 flight-planning forecasts. Real-time forecasts used WRF version 2.2.1 and were run with 45-km
157 and 15-km grid spacing for single deterministic forecasts (D1 and D2 in Fig. 1) and 45-km grid
158 spacing for ensemble prediction (D1 only). The model was initialized with a 30-member
159 mesoscale ensemble-based multi-physics data assimilation system (Zhang et al. 2006; Meng and
160 Zhang 2008a,b) and assimilated standard radiosonde observations. The real-time WRF forecasts
161 were archived at the START08 field catalog ([http://catalog.eol.ucar.edu/cgi-](http://catalog.eol.ucar.edu/cgi-bin/start08/model/index)
162 [bin/start08/model/index](http://catalog.eol.ucar.edu/cgi-bin/start08/model/index)). The flight track of RF02 was assigned to fly across the jet exit region
163 and gravity wave active area predicted by the real-time forecasts (also see Fig. 11 in Pan et al.
164 2010 for the real-time mesoscale forecast of gravity waves). Higher-resolution post-mission

165 WRF simulations with 5-km and 1.67-km grid spacing (D3 and D4 in Fig. 1) were also
166 conducted to examine the role of small-scale dynamical processes (e.g., convection and gravity
167 waves), which will be briefly reported in section 3. Nevertheless, an in-depth investigation of the
168 gravity wave dynamics based on the high-resolution post-mission WRF simulations is beyond
169 the scope of the current study, and will be reported elsewhere.

170

171 **3. Overview of the flight-level measurements**

172 Figure 2 depicts the track design of the entire flight and five flight segments during RF02,
173 along with the horizontal wind speed and the smoothed horizontal divergence near the flight
174 level simulated by the high-resolution post-mission WRF simulations valid at different
175 representative times of each five segments. Three flight segments pass mainly along an upper-
176 tropospheric jet streak. These are labeled J1, J2, and J3 and are displayed in Fig. 2b, 2c, and 2d,
177 respectively. Two other flight segments cross the mountains and high plains of Colorado and
178 Kansas. These are labeled M1 and M2 and are displayed in Fig. 2e and 2f, respectively. Flight
179 segment J3 is the longest during RF02. That segment includes flight through or above: the jet
180 core (gray shading in Fig. 2), a jet over high mountains (see the terrain map in Fig. 1), the exit
181 region of the jet, and a surface cold front (not shown). The other two segments, J1 and J2, were
182 intended to be a single segment, but an altitude change was necessary due to air traffic control.

183 Guided by the WRF model forecasts (e.g., Fig. 11 in Pan et al. 2010), this GV flight
184 mission sampled WRF-predicted gravity waves with different potential sources including
185 imbalance of jet streak and orographic forcing. Figure 3 shows the along-track horizontal
186 velocity component (u), across-track horizontal velocity component (v), horizontal wind speed
187 (V ; $V = \sqrt{u^2 + v^2}$), vertical velocity component (w), potential temperature (θ), corrected static

188 pressure (p_c), static pressure (p_s), hydrostatic pressure correction (p_h) derived from the airborne
189 *in-situ* measurements as well as flight height, and terrain along each of the five flight segments.
190 To facilitate spectral and wavelet analyses of these measurements, each variable from the 1-Hz
191 aircraft measurement along the flight segment is linearly interpolated into 250-m spatial series
192 with fixed resolution in distance. The right-hand rule is used to determine the relationships
193 among the positive along-track directions, the positive across-track directions, and the positive
194 vertical directions. For segments J1, J2, and J3, the positive along-track (across-track) directions
195 are all approximately toward the northeast (northwest). For segments M1 and M2, the positive
196 along-track (across-track) directions are both approximately toward the east (north). The
197 corrected static pressure p_c is calculated using the formula of Smith et al. (2008, their equation
198 12):

$$199 \quad p_c = p_s + p_h = p_s + \bar{\rho}g(z - z_{ref}) \quad (1)$$

200 where z is the GPS altitude, z_{ref} is the average altitude of flight segment and $\bar{\rho}$ is the average
201 density of flight segment. Corrected static pressure p_c from equation 1 is to correct the measured
202 static pressure p_s to a common height level (i.e., z_{ref}) based on the assumption of local
203 hydrostatic balance. Smith et al. (2008) suggests that the contribution of p_s to p_c is much smaller
204 than p_h , because it is assumed that the aircraft almost flies on an isobaric surface.

205 Consistent with what was predicted by the real time WRF forecast guidance (as shown in
206 Fig.11 of Pan et al. 2010) as well as simulated by the high-resolution post-mission WRF
207 simulations (in particular the horizontal divergence as potential signals of gravity waves as
208 shown in Fig. 2), the GV *in-situ* measurements of different atmospheric variables suggest there
209 are prevalent gravity wave activities along almost every leg of the 8-hr flight, most notably in the
210 vertical motion field. The largest amplitude of w ([over 2 m/s](#)) is during the middle portion of

211 segment J3 ([location 680-780 km](#)) on the lee slopes of the Rocky Mountains, ([also see the](#)
212 [discussion in section 5.2](#)). The high terrain and the lee slopes also have the enhanced vertical
213 motions for both segment M1 and segment M2. Though not as large in amplitude, enhanced
214 fluctuations of vertical motions are also observed in the northern end of segment J3, which is in
215 the exit region of the upper-level jet streak and above the surface front. [The enhanced variances](#)
216 [of vertical motion, accompanied by the changes in horizontal wind and potential temperature,](#)
217 [may be associated with topography for both M1 and M2 segments, even though the role of jet](#)
218 [cannot be isolated.](#)

219 Power spectra of five selected aircraft measurement variables are given in Fig. 4 for each
220 of the five flight segments during RF02. [The calculations of the spectra are performed with the](#)
221 [“specx_anal” function in the NCAR Command Language \(NCL\). Several steps are done before](#)
222 [the calculations. Firstly, the mean and least squares linear trend in each of the series are](#)
223 [removed. Secondly, smoothing by averaging 7 periodogram estimates is performed. Thirdly,](#)
224 [10% of the series are tapered.](#) For segment J1, u , v , θ and p_c have several significant spectral
225 peaks for wavelengths ranging from 16-128 km (mesoscales). The statistically significant
226 spectral peaks in w are more for smaller scales, one at 2-4 km, and the other at 8-32 km. The
227 spectral characteristics for segment J2 are mostly the same as J1 except for much less power at
228 longer wavelengths (16-128 km) and only one peak at smaller scales (2-8 km). For segment J3,
229 both u and θ have statistically significant spectral peaks at mesoscales (~50 and 128 km) and at
230 smaller scales (8-16 km), the later (not the former) of which is also very pronounced for the w
231 spectrum. No significant spectral peak is found for the corrected static pressure p_c for segment
232 J3, except at 512 km, which is likely a reflection of the sub-synoptic scale pressure patterns at
233 the flight level (Fig. 2d). For segment M1, there is a significant mesoscale spectral peak at

Fuqing Zhang 4/25/2015 9:52 AM

Deleted: .

Fuqing Zhang 4/25/2015 9:52 AM

Deleted: .

Fuqing Zhang 4/25/2015 9:52 AM

Formatted: Indent: First line: 0.5"

236 around 32-64 km for u , θ and p_c , while smaller-scale variations from 4-16 km are also
237 significant for nearly all variables except for p_c . There are almost no significant spectral peaks
238 for all 5 variables for segment M2 except for around 2 km for w .

239 Past studies from both aircraft observations (e.g., Nastrom and Gage 1985; Bacmeister et
240 al. 1996; Lindborg 1999) and numerical simulations (e.g., Skamorcok 2004; Waite and Snyder
241 2013) have revealed/verified the existence of an approximate $-5/3$ power law that is expected for
242 the direct energy cascade in isotropic three-dimensional turbulence (e.g., Kolmogorov 1941) and
243 the inverse cascade in two dimensions (e.g., Kraichnan 1967), as well as an approximate -3
244 power law that is expected for quasigeostrophic turbulence theory (e.g., Charney 1971). The
245 spectral slopes of different variables derived from the flight-level measurements from START08
246 are thus examined here in detail. Overall in segment J3, the spectrum slope for θ (the third
247 column in Fig. 4d) is remarkably similar to those for u (the third column in Fig. 4a) and v (the
248 third column in Fig. 4b), except that there appears to be a deviation from both -3 and $-5/3$ power
249 laws for scales of $\sim 8\sim 16$ km. The spectral slope of w (the third column in Fig. 4c) is also similar
250 to that of θ (the third column in Fig. 4d) for all scales below 32 km, including the above-
251 mentioned deviation. However, for scale larger than ~ 32 km, the slope of w (the third column in
252 Fig. 4c) quickly dropped to almost zero, which is consistent with the continuity equation for
253 near-balanced non-divergent large-scale motions.

254 There are also similarities and differences in spectral slopes among different flight
255 segments depicted in Fig. 4. For example, the above-mentioned spectral shapes of u and v from
256 segment J3 are similar to those from segment J2 (i.e., the second and third columns in Fig. 4a
257 and Fig 4b). Such consistent signals probably result from sampling under similar large-scale
258 background flow at similar flight altitude with almost identical topography, especially between

259 the adjacent flight segments J1+J2 and J3. Despite the overall resemblance among the flight
260 segments of RF02, there are some unique characteristics in the power spectral distributions for
261 individual segments. For segments M1 and M2, for example, (i.e., the fourth column versus the
262 fifth column in Fig. 4), the slopes of u and v during segment M1 are approximately consistent
263 with a -3 power law for the scale of $\sim 0.5\text{--}8$ km, while those during segment M2 follows a $-5/3$
264 power law instead. This is probably associated with the fact that segment M2 successfully
265 captures a rapid decrease in u (from ~ 65 m/s to ~ 40 m/s) while segment M1 has no such a
266 dramatic reduction in u (the fourth column in Fig. 3a versus the fifth column in Fig. 3a). Note
267 that the aircraft during segment M1 flew away from the jet core region, as the jet was still
268 moving eastward to the downhill side of the topography. In contrast, the aircraft during segment
269 M2 flew directly toward the approaching jet core at a lower flight level than segment M1 (the
270 fourth column in Fig. 3d versus the fifth column in Fig. 3d), and the observed decline of u (i.e., a
271 potential jet exit region) is located roughly on the downhill side of the topography (the fifth
272 column in Fig. 3d). This suggests that the spectral slopes for the aircraft measurements can, in
273 fact, be extremely sensitive to changes in the background flow, even though sampling takes place
274 in the same area only a few hours apart.

275 Figure 5 shows composite spectra for eight selected variables averaged over 68 flight
276 segments. Unsurprisingly, the composite spectra are much smoother due to averaging. For u
277 (Fig. 5a), v (Fig. 5b), and horizontal wind speed V (Fig. 5d), the slope of the power spectra are
278 consistent with a $-5/3$ power law for scales above $\sim 8\text{--}16$ km. For w (Fig. 5c), its spectral slope
279 is generally consistent with -3 power laws for the scale of $\sim 0.5\text{--}2$ km but is nearly zero for
280 scales over 32 km, while the slopes in between ($\sim 2\text{--}32$ km) appear to follow an approximate -
281 $5/3$ power law, with a statistically significant spectral peak at $\sim 8\text{--}16$ km. Even though the kinetic

Fuqing Zhang 4/25/2015 9:52 AM

Deleted: 5c

Fuqing Zhang 4/25/2015 9:52 AM

Deleted: 5d

Fuqing Zhang 4/25/2015 9:52 AM

Deleted: For θ

285 [energy spectra \(Fig. 5e\)](#) may show a -5/3 slope that covers a larger range, the -3 slope over small
 286 [scale in KE is still evident. For \$\theta\$ \(Fig. 5f\)](#) at scales between ~0.5 km and ~2 km, its slope also
 287 obeys a -3 power law. For θ (Fig. 5f) at the scale greater than ~8~16 km, the slope of power
 288 spectrum tends to have a -5/3 slope, which is similar to u (Fig. 5a), v (Fig. 5b), and V (Fig. 5d)
 289 for the same scales. For all the three pressure-related variables (i.e., p_c in Fig. 5g, p_s in Fig. 5h,
 290 p_h in Fig. 5i), their slopes generally fall around a -5/3 power law, except for scales less than ~4
 291 km in p_h (Fig. 5i). However, it is noteworthy that there is a sudden concavity (convexity) in p_c
 292 (p_s or p_h) for scales between ~4 km and ~16 km (also see the discussion in section 5.3).

Fuqing Zhang 4/25/2015 9:52 AM
Deleted: 5e

Fuqing Zhang 4/25/2015 9:52 AM
Deleted: 5e

Fuqing Zhang 4/25/2015 9:52 AM
Deleted: 5c

Fuqing Zhang 4/25/2015 9:52 AM
Deleted: 5f

Fuqing Zhang 4/25/2015 9:52 AM
Deleted: 5g

Fuqing Zhang 4/25/2015 9:52 AM
Deleted: 5h

Fuqing Zhang 4/25/2015 9:52 AM
Deleted: 5h

294 4. Wavelet analysis

295 4.1 Single-variable wavelet analysis

296 Standard spectral analysis methods characterize the variance as a function of wavelength
 297 for an entire data record (flight segment), but do not indicate where variance of a particular
 298 wavelength is located within the data record. We use wavelet analysis to complement the
 299 spectral analysis in section 3 to study the variance as a function of wavelength within the five
 300 flight segments from RF02. A Morlet wavelet function is employed in this study (e.g., Torrence
 301 and Compo 1998; Zhang et al. 2001; Woods and Smith 2010). This is a continuous wavelet
 302 transform that uses non-orthogonal complex wavelet functions comprising a plane wave
 303 modulated by a Gaussian function (e.g., equation 1 in Torrence and Compo 1998):

$$304 \quad \psi_0(\eta) = \pi^{-1/4} e^{i\omega_0\eta} e^{-\eta^2/2} \quad (2)$$

305 where ω_0 is the dimensionless wave number and η is the dimensionless distance. Here ω_0 is set
 306 to 6 to satisfy the admissibility condition (Farge 1992). The continuous wavelet transform, used

314 to extract localized spectral information, is defined as the convolution of the series of interest x
315 with the complex conjugate of the wavelet (e.g., equation 2 in Torrence and Compo 1998)

316
$$W_n(s) = \sum_{n'=0}^{N-1} x_{n'} \psi^* \left[\frac{(n'-n)\Delta x}{s} \right] \quad (3)$$

317 where $*$ is the complex conjugate, n is the localized position index, s is the wavelet scale, and
318 Δx is the resolution of the data (0.25 km in this case). The cone of influence (COI) shows the
319 region of the wavelet spectrum where the edge errors cannot be ignored. Computation of the
320 wavelet spectrum and edge error is performed with the wavelet function of equation 3 (Torrence
321 and Compo 1998) in [NCL](#).

322 Figure 6 contains the wavelet power spectra of five selected observed variables along the
323 five selected flight segments of RF02. Using the long segment J3 as an example again (third
324 column in Fig. 6), there is a substantial peak in the power of u (Fig. 6a) at wavelengths around
325 128-km between 400 and 700 km along the flight leg (also seen in p_c of Fig. 6e); ~100-km wave
326 power peaks at location 100-300 km; the wave power of wavelength from ~64 km to ~128 km
327 also peaks at location 1200-1400 km. The greatest similarity is between the spectra of w and θ
328 (Figs. 6c and d). For example, from location 100 km to 800 km during segment J3, local
329 maximum of power in w (the third column in Fig. 6c) resembles the one in θ (the third column
330 in Fig. 6d). In particular, three distinguished wave modes (~64 km, ~32 km, and ~10 km in
331 along-track wavelength) collocate at location 600-800 km (downstream of a localized hill around
332 600 km in the third column of Fig. 3d). Relatively persistent ~10-km waves in w are shown at
333 location 200-700 km, which corresponds to a similar peak in the spectral analysis of w in the
334 third column of Fig. 4c. Note that such ~10-km waves are also found in other flight segments in
335 RF02 (e.g., location 0-600 km during segment M1, the fourth column in Fig. 6c) and other

Fuqing Zhang 4/25/2015 9:52 AM
Deleted: the NCAR Command Language (NCL).

338 research flights in START08 (not shown). Interpretations of such small-scale localized wave
 339 | variances, as well as mesoscale localized wave variances, are discussed in section 5.

340

341 4.2 Polarization relationships from cross-wavelet analysis

342 Following Woods and Smith (2010), the phase relationship between two variables (e.g., u
 343 and v , hereafter in short noted as $(u'v')_p$) can be determined from the cospectrum $(u'v')_c$ and
 344 quadrature spectrum $(u'v')_q$, which are defined as (also see section 6c in Torrence and Compo
 345 1998; equation 8 and appendix A in Woods and Smith 2010):

$$346 \quad (u'v')_c = \text{Re}\{U_n(s_j)V_n^*(s_j)\} \quad (4)$$

$$347 \quad (u'v')_q = \text{Im}\{U_n(s_j)V_n^*(s_j)\} \quad (5)$$

348 where U_n and V_n represent the wavelet transforms of u and v from equation 3, $U_n(s_j)V_n^*(s_j)$ is
 349 the complex-valued cross-wavelet spectrum, while $\text{Re}\{ \}$ and $\text{Im}\{ \}$ represent the real and
 350 imaginary parts of the variables inside the parentheses, respectively. Woods and Smith (2010)
 351 focus on the energy flux by analyzing $(p_c'w')_c$ from equation 4 for vertically propagating waves
 352 and $(p_c'w')_q$ from equation 5 for vertically trapped/ducted waves. In principle, $(p_c'w')_p$ should
 353 be, theoretically speaking, associated with $(u'w')_p$ ($(v'w')_p$) (e.g., Eliassen and Palm 1960;
 354 Lindzen 1990). This is particularly true for stationary mountain waves, which may be present for
 355 RF02 given complex topography during each of the flight segments. However, in practice,
 356 Woods and Smith (2010, their section 7) argued that the perturbation longitudinal velocity was
 357 noisier than pressure in their study. In addition to equation 4 and equation 5, one can also define
 358 the absolute coherence phase angle as $\frac{180}{\pi} \times \arctan\left(\left|\frac{\text{Im}\{U_n(s_j)V_n^*(s_j)\}}{\text{Re}\{U_n(s_j)V_n^*(s_j)\}}\right|\right)$ (also see section 6d in
 359 Torrence and Compo 1998).

360 The phase relations among multiple variables are examined to further explore whether the
361 enhanced variances from the spectral and wavelet analyses are vertically propagating gravity
362 waves. Figure 7 shows three selected examples of cospectrum analysis (i.e., $(u'w')_c$ in Fig. 7a,
363 $(v'w')_c$ in Fig. 7b, $(p_c'w')_c$ in Fig. 7c), one selected example of quadrature spectrum analysis
364 (i.e., $(\theta'w')_q$ in Fig. 7d), and one example of absolute coherence phase angle for $(\theta'w')_p$ (Fig.
365 7e). In the case of a single monochromatic internal gravity wave propagating vertically, for
366 $(u'w')_c$ (Fig. 7a), positive (negative) values indicate upward (downward) flux of along-track
367 momentum. For $(v'w')_c$ (Fig. 7b), positive (negative) values indicate upward (downward) flux
368 of across-track momentum. For $(p_c'w')_c$ (Fig. 7c), positive (negative) values indicate positive
369 (negative) vertical energy transport. For the quadrature spectrum of $(\theta'w')_q$ (Fig. 7d), values
370 should be nonzero while the absolute coherence phase angle of $(\theta'w')_p$ (Fig. 7e) should be close
371 to 90 degree.

372 We again take segment J3 as an example (the third column in Fig. 7): for the small-scale
373 component with along-track wavelength less than 50 km (horizontal solid line), enhanced but
374 incoherent variances are detected for location 100-500 km and for location 600-800 km, with
375 fluctuating positive and negative values for both $(u'w')_c$ (the third column in Fig. 7a) and
376 $(v'w')_c$ (the third column in Fig. 7b). [The variations in the signs of vertical transports of
377 horizontal momentum fluxes imply that this flight segment is sampling waves propagating in
378 both forward and backward direction, assuming the vertical energy transports are generally
379 upward.](#) Correspondingly, the absolute coherence phase angle for $(u'v')_p$ (not shown) also
380 alternates frequently between nearly 0 degree and nearly 90 degree. In particular, some of the
381 enhanced variances in the cospectra for along-track wavelengths from ~4 km to ~16 km, though
382 fluctuating in signs, are significant above the 95% confidence level.

383 For the mesoscale component with wavelengths from ~50 to ~100 km, remarkable
384 localized quadrature variance is found in $(\theta'w')_q$ (the third column in Fig. 7d) for location 500-
385 800 km, consistent with the wavelet analysis of w in the third column of Fig. 6c and θ in the
386 third column of Fig 6d. The absolute coherence phase angle for $(\theta'w')_p$ in Fig. 7e also
387 demonstrate that the cross-wavelet spectrum between θ and w is mostly dominated by their
388 quadrature spectrum (red color shading in Fig. 7e), though there are some exceptions (blue color
389 shading in Fig. 7e).

390 The similarities/discrepancies among different wavelet cospectra and quadrature spectra
391 examined in Fig. 7 demonstrate the difficulties in gravity wave identification and the
392 uncertainties in gravity wave characteristics estimation based solely on aircraft measurements.

393 In addition to cross-wavelet analysis, the signs of the net fluxes (e.g., $\overline{u'w'}$, $\overline{v'w'}$, and
394 $\overline{w'p_c'}$) at each wavelength can also be estimated by the cospectrum analysis based on Fourier
395 transform over the entire segment (not shown). Generally speaking, for the scale below ~32 km,
396 both positive values and negative values are important in $\overline{u'w'}$ and $\overline{v'w'}$, while positive $\overline{w'p_c'}$
397 appears to be more continuous than negative $\overline{w'p_c'}$. For the scale above ~32 km, negative $\overline{u'w'}$
398 (positive $\overline{w'p_c'}$) appears to be more continuous than positive $\overline{u'w'}$ (negative $\overline{w'p_c'}$), while there
399 is no dominant sign for $\overline{v'w'}$ one way or the other.

400

401 5. Selected Wave-like Examples: signal of gravity waves or measurement noise?

402 This section examines several examples of wave-like variations during segment J3 in
403 more detail. Bandpass-filtered values of selected variables are computed by synthesizing the

Fuqing Zhang 4/25/2015 9:52 AM

Formatted: Font:Not Bold

Fuqing Zhang 4/25/2015 9:52 AM

Formatted: Font:Times New Roman

404 wavelet transform using wavelets with scales between j_1 and j_2 using (e.g., equation 29 in
 405 Torrence and Compo 1998)

$$406 \quad x_n' = \frac{\Delta j \Delta x^{1/2}}{C_\delta \psi_0(0)} \sum_{j=j_1}^{j_2} \frac{Re\{W_n(s_j)\}}{s_j^{1/2}} \quad (6)$$

407 where Δj is the scale resolution and C_δ is a reconstruction factor taken as 0.776 for Morlet
 408 wavelet. The wavelet-based filter in equation 6 has the advantage in removing noise at each
 409 wave number and isolating single events with a broad power spectrum or multiple events with
 410 different wave number (Donoho and Johnstone 1994; Torrence and Compo 1998).

411 Nine pairs of variables, including $(u'w')_p$, $(v'w')_p$, $(u'v')_p$, $(p_c'u')_p$, $(p_c'v')_p$,
 412 $(p_c'w')_p$, $(\theta'w')_p$, $(p_s'w')_p$, and $(p_h'w')_p$, are selected to examine whether the phase
 413 relationship of the variations in the airborne measurements is consistent with the linear theory for
 414 gravity waves. Generally speaking, the phase relation between two variables can be classified
 415 into two major categories: 1) In-phase or out-of-phase relationships, in which one variable leads
 416 or lags the other variable by approximately 0° or 180° ; 2) Quadrature relationships, in which one
 417 variable leads or lags the other by approximately 90° .

418 The phase relationships for linear gravity waves are determined by theory and their
 419 propagation characteristics. Take $(u'w')_p$, $(v'w')_p$, and $(p_c'w')_p$ as examples, if they have an
 420 in- or out-of-phase relationship, the waves are propagating in the vertical direction; if they have a
 421 quadrature relationship, the waves do not propagate vertically and may be trapped or ducted.
 422 Take $(u'v')_p$ as another example, if they have an in- or out-of-phase relationship, the waves may
 423 be internal gravity waves whose intrinsic frequencies are much higher than the Coriolis
 424 frequency; if they have a quadrature relationship, the waves may be inertio-gravity waves with
 425 intrinsic frequencies close to the Coriolis frequency. For vertically propagating linear gravity
 426 waves, $(\theta'w')_p$ should have a quadrature relationship. According to Smith et al. (2008), p_h'

427 should dominate over p_s' , if the aircraft almost flies on a constant pressure surface.
428 Consequently, $(p_h'w')_p$ should be almost identical to $(p_c'w')_p$.

429

430 *5.1 Examples of mesoscale wave variances*

431 Figure 8 demonstrates an example of potential mesoscale gravity waves selected based on
432 the wavelet analysis of u (Fig. 6a), w (Fig. 6c), θ (Fig. 6d), and p_c (Fig. 6e) for location 250-360
433 km in segment J3 (the exit region of northwesterly jet in Fig. 2d). The wave signals are further
434 highlighted by applying a wavelet-based filter (i.e., equation 6) to extract wavelike variations
435 with along-track wavelength between 100 and 120 km. Panels a, b, d, and e show out-of-phase
436 relationships for $(u'w')_p$, $(v'w')_p$, $(p_c'u')_p$, and $(p_c'v')_p$ respectively; while panels c, f, and i
437 show in-phase relationships for $(u'v')_p$, $(p_c'w')_p$, and $(p_h'w')_p$. Panels g and h show
438 quadrature relationships for $(\theta'w')_p$ and $(p_s'w')_p$. The observed phase relations shown in Fig. 8
439 are generally consistent with linear theory for propagating monochromatic gravity waves, as
440 indicated by the cospectrum/quadrature spectrum analysis in Fig. 7. These signals are likely to be
441 internal gravity waves (due to the in-phase relation of $(u'v')_p$ in Fig. 8c) with positive vertical
442 group velocity (due to their positive vertical energy flux, Fig. 8f).

443 In contrast, Figure 9 is an example of wave-like disturbances that lacks a clear,
444 propagating, linear-wave, phase relationship. This example is also selected based on the wavelet
445 analysis of segment J3 for u , v , and p_c (Figs. 6a, b, and e) for along-track wavelength near 128
446 km and location between 560 and 688 km along the segment. This segment lies above the
447 complex topography as depicted in the third column of Fig. 3d. According to Figs. 9a-9e,
448 $(u'w')_p$, $(u'v')_p$, and $(p_c'u')_p$ seem to have out-of-phase relationships, while $(v'w')_p$ and
449 $(p_c'v')_p$ have almost perfect in-phase relationships. These phase relationships appear to be

450 reasonable and generally consistent with the linear theory. The near in-phase relationship
451 exhibited by $(\theta'w')_p$ (Fig. 9g), however, raises doubts about whether these variations are true
452 gravity waves, as this is not consistent with linear theory. If they are in fact gravity wave signals,
453 the discrepancy highlights the difficulties of extracting gravity wave perturbations from
454 observations. For example, the mesoscale variances may be contaminated by small-scale
455 variability of θ and w due to the coexistence of wave variances at different scales for this region
456 (see the wavelet analysis of w in Fig. 6c in and θ in Fig. 6d). Additionally, there are uncertainties
457 in extracting mesoscale gravity waves from a varying background flow (e.g., Zhang et al. 2004),
458 especially for u , v and θ . Note that θ and w have a very consistent quadrature relation from ~ 8
459 km to ~ 64 km for this region in their quadrature spectrum of Fig. 7d (also see Fig. 7e), but this
460 quadrature relation (the third column in Fig. 7d), including their corresponding wavelet spectrum
461 (the third column in Fig. 6c and Fig. 6d) is much weaker for wavelengths near 128 km for
462 location 560-688 km in segment J3.

463 Consistent with Smith et al. (2008), the amplitude of p_h' is much larger than the
464 amplitude of p_s' for both examples of mesoscale wave variances. Therefore, $(p_h'w')_p$ is almost
465 identical to $(p_c'w')_p$ for both cases (Fig. 8f versus Fig. 8i; Fig. 9f versus Fig. 9i). It appears that
466 the assumption of constant p_s flight height is valid for these two mesoscale examples.

467

468 *5.2 Examples of small-scale wavelike variations*

469 Figure 10 shows an example of short-scale wave-like disturbances that have a phase
470 relationship consistent with linear gravity wave theory based on the wavelet analysis in Fig. 6
471 with scales from 32 to 64 km located at 650 to 750 km during segment J3. In-phase relationships
472 are seen in the filtered signals of $(p_c'v')_p$ (Fig. 10e), while out-of-phase relationships are seen in

473 $(u'v')_p$ and $(p_c'u')_p$ (Figs. 10c and d). Quadrature relationships can generally be seen in
474 $(u'w')_p$, $(v'w')_p$, $(p_c'w')_p$, and $(\theta'w')_p$ (Figs. 10a, b, f, and g). These small-scale waves have
475 no apparent vertical flux of horizontal momentum (Figs. 10a and b) and no vertical energy flux
476 (Fig. 10f), a key sign of vertically trapped gravity waves. Short-scale waves based on GV aircraft
477 measurements and/or numerical simulations are also discussed in Smith et al. (2008), Woods and
478 Smith (2010; 2011).

479 However, parts of the small-scale wave variations derived from the *in-situ* measurements,
480 especially for wavelengths from 5 to 15 km, may be difficult to classify as gravity waves. Figure
481 11 shows an example of short-scale wave variations in the aircraft measurements with along-
482 track wavelengths from 8 to 16 km for locations 680 to 780 km along segment J3. As depicted in
483 Fig. 11, $(u'w')_p$ (Fig. 11a) appears to have a quadrature relationship, even though this relative
484 phase varies, especially for locations from 710 to 730 km. Compared to $(u'w')_p$ (Fig. 11a),
485 $(v'w')_p$ and $(\theta'w')_p$ (Fig. 11b and g) have consistent quadrature relationships within this 100-
486 km distance. On the other hand, $(u'v')_p$ (Fig. 11c) varies significantly from one wavelength to
487 the next. The amplitude of w' in this example is extremely large (~ 2.5 m/s at its maximum) in
488 this selected example. In comparison, the amplitude of p_c' is rather small, and it is actually too
489 small to be noticed when using a wider bandpass window (not shown). Also, the quadrature
490 relationship in $(p_c'w')_p$ (Fig. 11f) is not as remarkable as those in $(u'w')_p$ and $(v'w')_p$ (Figs.
491 11a and b), which appears to contradict the theoretical description of Eliassen and Palm (1960)
492 on energy and momentum fluxes (also see Lindzen 1990). In addition, it is worth mentioning that
493 $(p_s'w')_p$ and $(p_h'w')_p$ in Figs. 11h and i have almost perfect out-of-phase and in-phase
494 relationships, respectively.

495 In contradiction to Smith et al. (2008), the amplitude of p_h' in the above example of Fig.
 496 11 is comparable with the amplitude of p_s' (Fig. 11h versus Fig. 11i). Surprisingly, $(p_c'w')_p$,
 497 $(p_s'w')_p$, and $(p_h'w')_p$ are also very different from each other (compare Figs. 11f, h, and i). The
 498 signals of p_s' and p_h' (Fig. 11h and i) are out-of-phase for wavelengths near 10 km and have
 499 comparable amplitude, which leads to nearly no such wave variances in p_c' (Fig. 11d-11f) given
 500 p_c' is the sum of p_s' and p_h' .

501

502 *5.3 Insight from spectral analysis of different pressure variables*

503 Figure 12a compares the power spectrum of three pressure-related variables (i.e.,
 504 corrected static pressure p_c , static pressure p_s , hydrostatic pressure correction p_h ; also see
 505 equation 1). Using segment J3 as an example, for wavelengths greater than ~ 32 km, p_c is almost
 506 identical to p_h ; for wavelengths between ~ 32 km and ~ 4 km, the variances between p_s and p_h
 507 are comparable, and the variances of p_c are noticeably smaller than those in p_s and p_h ; for
 508 wavelengths less than ~ 4 km, p_c is almost identical to p_s . Figure 12b shows the quantity

509 $\sqrt{\frac{spec(p_s)+spec(p_h)}{spec(p_c)}}$, where $spec()$ indicates the power spectrum of the variable inside the

510 parentheses (e.g., Figs. 4-5). For segment J3, the square root of the ratio is close to 1.0 for the
 511 wavelengths greater than ~ 32 km and less than ~ 4 km. At intermediate wavelengths, the square
 512 root of the ratio reaches a maximum near 10 for wavelengths of ~ 10 km. This suggests that p_s'
 513 and p_h' may tend to cancel each other at intermediate scales, which reduces the amplitude of p_c'
 514 at these intermediate wavelengths (also see the example in Fig. 11) since p_c' is the sum of p_s'
 515 and p_h' . Similar behaviors can be also observed in other segments, although the exact ranges of
 516 the intermediate wavelengths may be different from case to case.

517 Figure 12 suggests that the assumption of constant p_s flight height may not be valid at all
518 scales, though it appears to be true for mesoscale waves. In consequence, p_h' may not always
519 dominate over p_s' as assumed in Smith et al. (2008). The spectral analysis and wavelet analysis
520 of p_s (not shown) demonstrate that p_s indeed has relatively large variances for the short-scale
521 range, and that p_s and w share some common characteristics (also see Fig. 3). Moreover, the
522 hydrostatic approximation, which is the underlying assumption for equation 1, may no longer be
523 valid for short scales.

524

525 6. Concluding remarks and discussion

526 One of the primary objectives of the recent START08 field experiment is to characterize
527 the sources and impacts of mesoscale waves with high-resolution flight-level aircraft
528 measurements and mesoscale models. The current study focuses on the second research flight
529 (RF02), which was the first airborne mission dedicated to probing gravity waves associated with
530 strong upper-tropospheric jet-front systems and high topography. Based on spectral and wavelet
531 analyses of the *in-situ* observations, along with a diagnosis of the polarization relationships, it is
532 found that there are clear signals of significant mesoscale variations with wavelengths ranging
533 from ~50 to ~500 km in almost every segment of the 8-hr flight (order ranging from 0.01 m/s to
534 1.0 m/s in vertical motion), which took place mostly in the lower stratosphere. The flow sampled
535 by the aircraft covers a wide range of background conditions including near the jet core, a jet
536 over the high mountains, and the exit region of the jet. In contrast, smaller-scale wavelike
537 oscillations below 50 km are found to be quite transient. In particular, aircraft measurements of
538 several flight segments are dominated by signals with sampled periods of ~20~60 seconds and
539 wavelengths of ~5~15 km (assuming that the typical flight speed is approximately 250 m/s).

Fuqing Zhang 4/25/2015 9:52 AM

Deleted: ,

Fuqing Zhang 4/25/2015 9:52 AM

Deleted: ,

542 This study suggests that at least part of the nearly-periodic high-frequency signals might
543 be unphysical and a result of intrinsic observational errors in the aircraft measurements or small-
544 scale flight-altitude fluctuations that are difficult to account for. Such potentially contaminated
545 variations are often collocated with larger-scale wave signals, which in turn may lead to larger
546 uncertainties in the estimation of the wave characteristics. Part of the uncertainties may come
547 from the inability of the aircraft to maintain constant static pressure altitude in the presence of
548 small-scale turbulence. The current study mainly focuses on examining the fluctuations with the
549 use of linear theory for monochromatic gravity waves. Therefore, in addition to measurement
550 errors, the possibilities that those fluctuations may be due to other physical phenomena (e.g.,
551 nonlinear dynamics, shear instability and/or turbulence) cannot be completely ruled out.
552 Nevertheless, despite the presence of possibly spurious wave oscillations in different flight
553 segments, the power spectra of horizontal winds and temperature averaged over many START08
554 flight segments generally follow the -5/3 power law. The common characteristics and individual
555 features of the wave variances and spectrum slope behaviors appear to be generally consistent
556 with past studies on the spectral analysis of aircraft measurement, including Nastrom and Gage
557 (1985) using the Global Atmospheric Sampling Program (GASP) flight dataset, and Lindborg
558 (1999) using the Measurement of Ozone and Water Vapor by Airbus In-Service Aircraft
559 (MOZAIC) aircraft observations. Spectral behaviors of atmospheric variables have also been
560 studied by high-resolution non-hydrostatic mesoscale numerical weather prediction (NWP)
561 models (e.g., Skamarock 2004; Tan et al. 2004; Zhang et al. 2007; Waite and Snyder 2013; Bei
562 and Zhang 2014).

563 Although the real-time mesoscale analysis and prediction system gave a reasonable
564 forecast guidance on the region of potential gravity wave activities, it remains to be explored (1)

Fuqing Zhang 4/25/2015 9:52 AM

Deleted: closely

566 how well the current generation of numerical weather models predicts the excitation of gravity
567 waves, (2) how often gravity waves break in the ExUTLS region, and (3) what evidence in tracer
568 measurements is shown for the contribution of gravity wave breaking to mixing. Future work
569 will also seek to examine the origin and dynamics of the gravity waves observed during RF02 of
570 START08 through a combination of observations and numerical modeling. This will help to
571 distinguish whether the sampled mesoscale and small-scale variances are gravity waves or
572 artifacts of the observing system.

573

574 **Acknowledgments:** The START08 experiment is sponsored by the National Science Foundation
575 (NSF). A large number of people contributed to the success of START08 experiment. The
576 dedication of the instrument team, co-sponsored by NCAR, University of Colorado, Harvard
577 University, University of Miami, Princeton University, NOAA Earth System Research
578 Laboratory (ESRL) Global Monitoring Division (GMD) and Chemical Science Division (CSD),
579 and the NCAR Research Aviation Facility staff in running the flight operation are the key factors
580 in the success of campaign. We also acknowledge the effort and skill of the GV pilots Henry
581 Boynton and Ed Ringleman, which was critical to meeting mission objectives. We benefit from
582 initial review comments from the editor Tim Dunkerton [and anonymous reviewers](#) on an earlier
583 version of the manuscript. This research is sponsored by NSF grants 0618662, 0722225,
584 0904635, and 1114849.

585 **References**

- 586 Alexander, M. J., and K. H. Rosenlof, 2003: Gravity-wave forcing in the stratosphere:
587 Observational constraints from the Upper Atmosphere Research Satellite and implications for
588 parameterization in global models. *J. Geophys. Res. – Atmos.*, 108: Art. No. 4597.
- 589 Bacmeister, J. T., S. D. Eckermann, P. A. Newman, L. Lait, K. R. Chan, M. Loewenstein, M. H.
590 Proffitt, and B. L. Gary, 1996: Stratospheric horizontal wavenumber spectra of winds, po-
591 tential temperature, and atmospheric tracers observed by high-altitude aircraft. *J. Geophys.*
592 *Res.*, 101, 9441–9470.
- 593 Bei, N., and F. Zhang, 2014: Mesoscale Predictability of Moist Baroclinic Waves: Variable and
594 Scale Dependent Error Growth. *Advances in Atmospheric Sciences*, doi: 10.1007/s00376-
595 014-3191-7.
- 596 Bertin F., Campistron B., Caccia J. L., Wilson R., 2001: Mixing processes in a tropopause
597 folding observed by a network of ST radar and lidar. *Annales Geophysicae*, 19, 953-963.
- 598 Bosart, L. F., W. E. Bracken, and A. Seimon, 1998: A study of cyclone mesoscale structure with
599 emphasis on a large-amplitude inertia-gravity waves. *Mon. Wea. Rev.*, 126, 1497-1527.
- 600 Brown, P. R. A., 1983: Aircraft measurements of mountain waves and their associated
601 momentum flux over the british isles. *Q. J. R. Meteorol. Soc.*, 109, 849-865.
- 602 Charney, J. G., 1971: Geostrophic turbulence. *J. Atmos. Sci.*, 28, 1087–1095.
- 603 Donoho, D. L., and I. M. Johnstone, 1994: Ideal spatial adaptation by wavelet shrinkage.
604 *Biometrika*, 81, 425–455.
- 605 Dornbrack, A., T. Birner, A. Fix, H. Flentje, A. Meister, H. Schmid, E. V. Browell, and M.
606 J. Mahoney, 2002: Evidence for inertia gravity waves forming polar stratospheric clouds
607 overscandinavia. *J. Geophys. Res.*, 107, 8287, doi:10.1029/2001JD000452.

608 Doyle, J., H. Volkert, A. Dornbrack, K. Hoinka, and T. Hogan, 2002: Aircraft measurements and
609 numerical simulations of mountain waves over the central Alps: A pre-MAP test case. *Q. J.*
610 *R. Meteorol. Soc.*, 128, 2175-2184.

611 Einaudi, F., A. J. Bedard, and J. J. Finnigan, 1989: A climatology of gravity waves and other
612 coherent disturbances at the Boulder Atmospheric Observatory during March–April 1984. *J.*
613 *Atmos. Sci.*, 46, 303–329.

614 Eliassen, A. and E. Palm, 1960: On the transfer of energy in stationary mountain waves. *Geophys.*
615 *Publ.*, 22, 1-23.

616 Farge, M., 1992: Wavelet transforms and their applications to turbulence. *Annu. Rev. Fluid*
617 *Mech.*, 24, 395-457.

618 Fritts, D. C., and G. D. Nastrom, 1992: Sources of mesoscale variability of gravity waves. Part
619 II: Frontal, convective, and jet stream excitation. *J. Atmos. Sci.*, 49, 111-127.

620 Gong, J., and M. A. Geller, 2010: Vertical fluctuation energy in United States high vertical
621 resolution radiosonde data as an indicator of convective gravity wave sources. *J. Geophys.*
622 *Res.* 115 (D11): 10.1029/2009JD012265.

623 Grivet-Talocia, S., F. Einaudi, W. L. Clark, R. D. Dennett, G. D. Nastrom, and T. E. VanZandt,
624 1999: A 4-yr Climatology of Pressure Disturbances Using a Barometer Network in Central
625 Illinois. *Mon. Wea. Rev.*, 127, 1613–1629.

626 Grubišić, V., J.D. Doyle, J. Kuettner, S. Mobbs, R.B. Smith, C.D. Whiteman, R. Dirks, S.
627 Czyzyk, S.A. Cohn, S. Vosper, M. Weissmann, S. Haimov, S.F.J. De Wekker, L.L. Pan, and
628 F.K. Chow, 2008: The Terrain-Induced Rotor Experiment. *Bull. Amer. Meteor. Soc.*, 89,
629 1513–1533.

630 Hertzog, A., and F. Vial, 2001: A study of the dynamics of the equatorial lower stratosphere by
631 use of ultra-long-duration balloons: 2. Gravity waves. *J. Geophys. Res.*, 106, 22 745– 22 761.

632 Jensen, E. J., D. Starr, and O. B. Toon, 2004: Mission investigates tropical cirrus clouds. *EOS*,
633 85, 45-50.

634 Kaplan, M. L., S. E. Koch, Y.-L. Lin, R. P. Weglarz, and R. A. Rozumalski, 1997: Numerical
635 simulations of a gravity wave event over CCOPE. Part I: The role of geostrophic adjustment
636 in mesoscale jetlet formation. *Mon. Wea. Rev.*, 125, 1185–1211.

637 Karacostas, T. S. and J. D. Marwitz, 1980: Turbulent kinetic energy budgets over
638 mountainousterrain. *J. Appl. Meteor.*, 19, 163-174.

639 Koch S.E., Jamison B.D., Lu C.G., Smith T.L., Tollerud E.I., Girz C., Wang N., Lane T.P.,
640 Shapiro M.A., Parrish D.D., Cooper O.R., 2005: Turbulence and gravity waves within an
641 upper-level front, *J. Atmos. Sci.*, 62, 3885-3908.

642 Koch, S. E., F. Zhang, M. Kaplan, Y.-L. Lin, R. Weglarz, and M. Trexler, 2001: Numerical
643 simulation of a gravity wave event observed during ccope. part 3: the role of a mountain-
644 plains solenoid in the generation of the second wave episode. *Mon. Wea. Rev.*, 129, 909–
645 932.

646 Kolmogorov, A. N., 1941: The local structure of turbulence in incompressible viscous fluid for
647 very large Reynolds number. *Dokl. Akad. Nauk SSSR*, 30, 301–305.

648 Koppel, L. L., L. F. Bosart, and D. Keyser, 2000: A 25-yr climatology of large-amplitude hourly
649 surface pressure changes over the conterminous United States. *Mon. Wea. Rev.*, 96, 51–68.

650 Kraichnan, R. H., 1967: Inertial ranges in two-dimensional turbulence. *Phys. Fluids*, 10, 1417–
651 1423.

652 Lane, T. P., J. D. Doyle, R. Plougonven, M. A. Shapiro, and R. D. Sharman, 2004: Ob-
653 servations and numerical simulations of inertia-gravity waves and shearing instabilities in the
654 vicinity of a jet stream. *J. Atmos. Sci.*, 61, 2692–2706.

655 Lane, T. P., M. J. Reeder, T. L. Clark, 2001: Numerical Modeling of Gravity Wave Generation
656 by Deep Tropical Convection. *J. Atmos. Sci.*, 58, 1249–1274.

657 Laursen, K. K., D. P. Jorgensen, G. P. Brasseur, S. L. Ustin, and J. R. Huning, 2006: HIAPER:
658 The next generation NSF/NCAR research aircraft. *Bull. Amer. Meteor. Soc.*, 87, 896-909.

659 Leutbecher, M. and H. Volkert, 2000: The propagation of mountain waves into the stratosphere:
660 Quantitative evaluation of three-dimensional simulations. *J. Atmos. Sci.*, 57, 3090-3108.

661 Lilly, D. K. and P. J. Kennedy, 1973: Observations of a stationary mountain wave and its
662 associated momentum flux and energy dissipation. *J. Atmos. Sci.*, 30, 1135-1152.

663 Lin, Y., and F. Zhang, 2008: Tracking gravity waves in baroclinic jet-front systems. *J. Atmos.*
664 *Sci.*, 65, 2402-2415.

665 Lindborg, E., 1999: Can the atmospheric kinetic energy spectrum be explained by two-
666 dimensional turbulence? *J. Fluid Mech.*, 388, 259 –288.

667 Lindzen, R. S., 1990: *Dynamics in Atmospheric Physics*. Cambridge University Press, 320 pp.

668 Meng, Z, and F. Zhang, 2008a: Test of an ensemble-Kalman filter for mesoscale and regional-
669 scale data assimilation. Part III: Comparison with 3Dvar in a real-data case study. *Mon. Wea.*
670 *Rev.*, 136, 522-540.

671 Meng, Z, and F. Zhang, 2008b: Test of an ensemble-Kalman filter for mesoscale and regional-
672 scale data assimilation. Part IV: Performance over a warm-season month of June 2003. *Mon.*
673 *Wea. Rev.*, 136, 3671-3682.

674 Mirzaei, M., C. Zülicke, A. Mohebalhojeh, F. Ahmadi-Givi, and R. Plougonven (2014),
675 Structure, energy, and parameterization of inertia–gravity waves in dry and moist simulations
676 of a baroclinic wave life cycle, *J. Atmos. Sci.*, 71, 2390–2414. doi:
677 <http://dx.doi.org/10.1175/JAS-D-13-075.1>
678 Moustouai, M., H. Teitelbaum, P. F. J. van Velthoven, and H. Kelder, 1999: Analysis of gravity
679 waves during the POLINAT experiment and some consequences for stratosphere-troposphere
680 exchange. *J. Atmos. Sci.*, 56, 1019-1030.
681 Nastrom, G. D., and D. C. Fritts, 1992: Sources of mesoscale variability of gravity waves. Part I:
682 Topographic excitation. *J. Atmos. Sci.*, 49, 101–110.
683 Nastrom, G. D., and K. S. Gage, 1985: A Climatology of Atmospheric Wavenumber Spectra of
684 Wind and Temperature Observed by Commercial Aircraft. *J. Atmos. Sci.*, 42, 950–960.
685 O’Sullivan, D. and T. J. Dunkerton, 1995: Generation of inertia-gravity waves in a simulated life
686 cycle of baroclinic instability. *J. Atmos. Sci.*, 52, 3695–3716.
687 Pan, L. L., K. P. Bowman, E. L. Atlas, S. C. Wofsy, F. Zhang, and co-authors, 2010:
688 Stratosphere-Troposphere Analyses of Regional Transport Experiment. *Bulletin of the*
689 *American Meteorological Society*, 91, 327-342.
690 Pavelin E., J.A. Whiteway, G. Vaughan, 2001: Observation of gravity wave generation and
691 breaking in the lowermost stratosphere. *J. Geophys. Res.*, 106 (D6), 5173-5179.
692 Plougonven, R. and C. Snyder, 2007: Inertia-gravity waves spontaneously generated by jets and
693 fronts. Part I: Different baroclinic life cycles. *J. Atmos. Sci.*, 64, 2502–2520.
694 Plougonven, R., and F. Zhang, 2014: Internal gravity waves from atmospheric jets and fronts.
695 *Reviews of Geophysics*, 52, doi: 10.1002/2012RG000419.

Fuqing Zhang 4/25/2015 9:52 AM

Deleted: doi:
<http://dx.doi.org/10.1175/JAS-D-13-075.1>

698 Plougonven, R., H. Teitelbaum, and V. Zeitlin, 2003: Inertia gravity wave generation by
699 tropospheric midlatitude jet as given by the fronts and atlantic storm-track experiment radio
700 soundings. *J. Geophys. Res.-Atmos.*, 108, 888–889.

701 Pokrandt, P. J., G. J. Tripoli, and D. D. Houghton, 1996: Processes leading to the formation of
702 mesoscale waves in the midwest cyclone of 15 december 1987. *Mon. Wea. Rev.*, 124, 2726–
703 2752.

704 Poulos, G. S., William Blumen, David C. Fritts, Julie K. Lundquist, Jielun Sun, Sean P. Burns,
705 Carmen Nappo, Robert Banta, Rob Newsom, Joan Cuxart, Enric Terradellas, Ben Balsley,
706 and Michael Jensen, 2002: CASES-99: A Comprehensive Investigation of the Stable
707 Nocturnal Boundary Layer. *Bull. Amer. Meteor. Soc.*, 83, 555–581.

708 Powers, J. G. and R. J. Reed, 1993: Numerical model simulation of the large-amplitude
709 mesoscale gravity-wave event of 15 December 1987 in the central United States. *Mon. Wea.*
710 *Rev.*, 121, 2285–2308.

711 Radok, U., 1954: A procedure for studying mountain effects at low levels. *Bull. Amer. Meteor.*
712 *Soc.*, 35/9, 412.

713 Ramamurthy, M. K., R. M. Rauber, B. Collins, and N. K. Malhotra, 1993: A comparative study
714 of large-amplitude gravity-wave events. *Mon. Wea. Rev.*, 121, 2951–2974.

715 Rauber, R. M., M. Yang, M. K. Ramamurthy, and B. F. Jewett, 2001: Origin, evolution, and
716 fine-scale structure of the St. Valentine’s Day mesoscale gravity wave observed during
717 storm-fest. Part I: Origin and evolution. *Mon. Wea. Rev.*, 129, 198–217.

718 Reeder, M. J., and M. Griffiths, 1996: Stratospheric inertia-gravity waves generated in a
719 numerical model of frontogenesis. II: Wave sources, generation mechanisms and momentum
720 fluxes. *Quart. J. Roy. Meteor. Soc.*, 122, 1175–1195.

721 Schneider, R. S., 1990: Large-amplitude mesoscale wave disturbances within the intense
722 midwest extratropical cyclone of 15 December 1987. *Wea. Forecasting*, 5, 533–558.

723 [Shapiro, M. A., and P. J. Kennedy, 1975: Aircraft Measurements of Wave Motions within](#)
724 [Frontal Zone Systems. *Mon. Wea. Rev.*, 103, 1050–1054. doi:](#)
725 [http://dx.doi.org/10.1175/1520-0493\(1975\)103<1050:AMOWMW>2.0.CO;2](http://dx.doi.org/10.1175/1520-0493(1975)103<1050:AMOWMW>2.0.CO;2)

726 Skamarock, W. C., 2004: Evaluating Mesoscale NWP Models Using Kinetic Energy Spectra.
727 *Mon. Wea. Rev.*, 132, 3019–3032.

728 Skamarock, W. C., J. B. Klemp, J. Dudhia, D.O. Gill, D. M. Barker, W. Wang, and J. G. Powers,
729 2005: A description of the Advanced Research WRF Version 2. NCAR technical note
730 468+STR, 88 pp.

731 Smith, R. B., 1976: The generation of lee waves by the blue ridge. *J. Atmos. Sci.*, 33, 507-519.

732 Smith, R. B., 1980: Linear theory of stratified hydrostatic flow past an isolated mountain. *Tellus*,
733 348-364.

734 Smith, R. B., B. K. Woods, J. Jensen, W. A. Cooper, J. D. Doyle, Q. Jiang, and V. Grubisic,
735 2008: Mountain waves entering the stratosphere. *J. Atmos. Sci.*, 65, 2543 –2562.

736 Tan, Z. M., F. Zhang, R. Rotunno, and C. Snyder, 2004: Mesoscale predictability of moist
737 baroclinic waves: Experiments with parameterized convection. *J. Atmos. Sci.*, 61, 1794-
738 1804.

739 Torrence, C., and G. P. Compo, 1998: A practical guide to wavelet analysis. *Bull. Amer. Meteor.*
740 *Soc.*, 19, 61 –78.

741 Uccellini, L. W. and S. E. Koch, 1987: The synoptic setting and possible source mechanisms for
742 mesoscale gravity wave events. *Mon. Wea. Rev.*, 115, 721–729.

743 Vaughan G, Worthington RM, 2000: Break-up of a stratospheric streamer observed by MST
744 radar. *Quarterly Journal of the Royal Meteorological Society*, 126, 1751-1769.

745 Vaughan, G., and R. Worthington, 2007: Inertia-gravity waves observed by the UK MST radar,
746 *Q. J. R. Meteorol. Soc.*, 133(S2), 179–188.

747 Vergeiner, I., and D. K. Lilly, 1970: The dynamic structure of lee wave flow as obtained from
748 balloon and airplane observations. *Mon. Wea. Rev.*, 98, 220-232.

749 Vincent, R. A., and M. J. Alexander, 2000: Gravity waves in the tropical lower stratosphere: An
750 observational study of seasonal and interannual variability. *J. Geophys. Res.*, 105, 17, 971-
751 17, 982.

752 Waite, M. L., and Chris Snyder, 2013: Mesoscale Energy Spectra of Moist Baroclinic Waves. *J.*
753 *Atmos. Sci.*, 70, 1242–1256.

754 Wang, L. and M. J. Alexander, T. P. Bui, and M. J. Mahoney, 2006: Small-scale gravity waves
755 in ER-2 MMS/MTP wind and temperature measurements during CRYSTAL-FACE. *Atmos.*
756 *Chem. Phys.*, 6, 1091-1104.

757 Wang, L., and M. A. Geller, 2003: Morphology of gravity-wave energy as observed from 4 years
758 (1998-2001) of high vertical resolution U.S. radiosonde data, *J. Geophys. Res.*, 108 (D16),
759 4489, doi:10.1029/2002JD002786.

760 Wang, S. and F. Zhang, 2007: Sensitivity of mesoscale gravity waves to the baroclinicity of jet-
761 front systems. *Mon. Wea. Rev.*, 135, 670-688.

762 Wei, J., and F. Zhang, 2014: Mesoscale gravity waves in moist baroclinic jet–front systems. *J.*
763 *Atmos. Sci.*, 71, 929–952. doi: <http://dx.doi.org/10.1175/JAS-D-13-0171.1>

764 Wei, J., and F. Zhang, 2015: Tracking gravity waves in moist baroclinic jet-front systems.
765 *Journal of Advanced Modeling in Earth Sciences (JAMES)*, DOI: 10.1002/2014MS000395

766 Woods, B. K. and R. B. Smith, 2010: Energy flux and wavelet diagnostics of secondary
767 mountain waves. *J. Atmos. Sci.*, 67, 3721-3738.

768 Woods, B. K. and R. B. Smith, 2011: Short-Wave Signatures of Stratospheric Mountain Wave
769 Breaking. *J. Atmos. Sci.*, 68, 635-656.

770 Wu, D. L., and F. Zhang, 2004: A study of mesoscale gravity waves over North Atlantic with
771 satellite observations and a mesoscale model. *J. Geophys. Res.-Atmos.*, 109, D22104.

772 Yamanaka, M. D., S. Ogino, S. Kondo, T. Shimomai, S. Fukao, Y. Shibagaki, Y. Maekawa, and
773 I. Takayabu, 1996: Inertio-gravity waves and subtropical multiple tropopauses: vertical
774 wavenumber spectra of wind and temperature observed by the MU radar, radiosondes and
775 operational rawinsonde network. *J. Atmos. Terr. Phys.*, 58, 785-805.

776 Zhang, F., 2004: Generation of mesoscale gravity waves in the upper-tropospheric jet-front
777 systems. *J. Atmos. Sci.*, 61, 440-457.

778 Zhang, F., and S. E. Koch, 2000: Numerical simulation of a gravity wave event over CCOPE.
779 Part II: Wave generated by an orographic density current. *Mon. Wea. Rev.*, 128, 2777– 2796.

780 Zhang, F., M. Zhang, J. Wei, and S. Wang, 2013: Month-Long Simulations of Gravity Waves
781 over North America and North Atlantic in Comparison with Satellite Observations. *Acta*
782 *Meteorologica Sinica*, 27, 446-454.

783 Zhang, F., N. Bei, R. Rotunno, C. Snyder, and C. C. Epifanio, 2007: Mesoscale predictability of
784 moist baroclinic waves: Convection-permitting experiments and multistage error growth
785 dynamics. *J. Atmos. Sci.*, 64, 3579-3594.

786 Zhang, F., S. E. Koch, and M. L. Kaplan, 2003: Numerical simulations of a large-amplitude
787 gravity wave event. *Meteorology and Atmospheric Physics*, 84, 199–216.

788 Zhang, F., S. E. Koch, C. A. Davis, and M. L. Kaplan, 2001: Wavelet analysis and the governing
789 dynamics of a large-amplitude gravity wave event along the east coast of the United States.
790 Q. J. R. Meteorol. Soc., 127, 2209-2245.

791 Zhang, F., S. Wang, and R. Plougonven, 2004: Uncertainties in using the hodograph method to
792 retrieve gravity wave characteristics from individual soundings. Geophysical Research
793 Letters, 31, L11110, doi:10.1029/2004GL019841.

794 Zhang, F., Z. Meng, and A. Aksoy, 2006: Tests of an ensemble Kalman filter for mesoscale and
795 regional-scale data assimilation. Part I: Perfect model experiments. Mon. Wea. Rev., 134,
796 722-736.

797 Zhang, S. D., and F. Yi, 2007: Latitudinal and seasonal variations of inertial gravity wave
798 activity in the lower atmosphere over central China, J. Geophys. Res., 112, D05109,
799 doi:10.1029/2006JD007487.

800

801

802 **Figure Captions**

803 **Figure 1.** The 68 Gulfstream V (GV) flight segments (colored lines) selected for wave analysis
804 during START08. The 18 colors represent 18 research flight (RF) missions. The thick blue lines
805 represent the second flight (RF02). The grey shadings give the terrain elevation map (shaded
806 every 250 m) over north America. The 4 black boxes are the model domain design for the second
807 research flight (RF02) during 21-22 April 2008, which are named D1-D4 from coarse to fine
808 domain with horizontal resolution as 45 km, 15 km, 5 km and 1.67 km, respectively. The field
809 catalog of the 18 RFs are available online (at
810 http://catalog.eol.ucar.edu/start_08/missions/missions.html). The GV ground tracks of the
811 18 RFs are also documented in Fig. 2 of Pan et al. (2010).

812
813 **Figure 2.** Simulated pressure at 9 km altitude (black contours; unit in hPa ; $\Delta = 2hPa$),
814 horizontal wind speed at 9 km altitude (black shadings; unit in ms^{-1} ; levels at 30, 40, 50, 60
815 ms^{-1}), and the mesoscale component of horizontal divergence at 12.5 km (blue contours,
816 positive; red contour, negative; contour levels at $\pm 7.5, \pm 15, \pm 30, \pm 60 \times 10^{-5} s^{-1}$) during RF02
817 in START08, with marked GV flight track (blue line) at selected time: (a) entire flight track at 21
818 April 18:00 UTC, (b) segment J1 at 21 April 19:10 UTC, (c) segment J2 at 21 April 19:50 UTC,
819 (d) segment J3 at 21 April 22:10 UTC, (e) segment M1 at 21 April 23:10 UTC, and (f) segment
820 M2 at 22 April 00:20 UTC. The triangle and circle marks represent the aircraft at the start time
821 of the segment and at selected time. The two-dimensional (2D) variables are based on D4 in Fig.
822 1. A band-pass filter is applied to extract signals with wavelength from 50 to 500 km for
823 horizontal divergence.

824

825 **Figure 3.** GV flight-level aircraft measurements during 5 selected segments (from left to right:
 826 J1, J2, J3, M1 and M2) of RF02 in START08: (a) along-track velocity component (red; unit in
 827 ms^{-1} ; left y axis), across-track velocity component (blue; unit in ms^{-1} ; right y axis) and
 828 horizontal velocity component (black; unit in ms^{-1} ; left y axis), (b) vertical velocity component
 829 (red; unit in ms^{-1} ; left y axis) and potential temperature (blue; unit in K ; right y axis), (c)
 830 perturbation of hydrostatic pressure correction (red; unit in hPa ; left y axis), static pressure
 831 (blue; unit in hPa ; right y axis) and corrected static pressure (black; unit in hPa ; left y axis), and
 832 (d) flight height (red; unit in km ; left y axis) and terrain (blue; black shading below terrain; unit
 833 in km ; right y axis). The series in segment J3 and M2 are reversed to facilitate the comparison
 834 with J1+J2 and M1, respectively. Therefore, the orientation of x axis is from west to east along
 835 each flight segment. The distance between minor tick marks in x axis is 100 km. The
 836 perturbations in (c) are defined as the differences between the original data and their mean from
 837 their corresponding segments.

838
 839 **Figure 4.** The spectrum (black line) of GV flight-level aircraft measurement during 5 selected
 840 segments (from left to right: J1, J2, J3, M1 and M2) of RF02 in START08: (a) along-track
 841 velocity component (unit: $m^2s^{-2} \cdot m$), (b) across-track velocity component (unit: $m^2s^{-2} \cdot m$), (c)
 842 vertical velocity component (unit: $m^2s^{-2} \cdot m$), (d) potential temperature (unit: $K^2 \cdot m$), and (e)
 843 corrected static pressure (unit: $hPa^2 \cdot m$). Green lines show the theoretical Markov spectrum and
 844 the 5% and 95% confidence curves using the lag 1 autocorrelation. The blue (red) reference lines
 845 have slopes of -5/3 (-3).

846

Fuqing Zhang 4/25/2015 9:52 AM
 Deleted: ,
 Fuqing Zhang 4/25/2015 9:52 AM
 Deleted: ,
 Fuqing Zhang 4/25/2015 9:52 AM
 Deleted: ,
 Fuqing Zhang 4/25/2015 9:52 AM
 Deleted: ,
 Fuqing Zhang 4/25/2015 9:52 AM
 Deleted: .

852 **Figure 5.** Composite spectrum (black line) of GV flight-level aircraft measurement averaging
853 over all 68 segments in START08 (colored lines in Fig. 1): (a) along-track velocity component
854 (unit: $m^2s^{-2} \cdot m$), (b) across-track velocity component (unit: $m^2s^{-2} \cdot m$), (c) vertical velocity
855 component (unit: $m^2s^{-2} \cdot m$), (d) horizontal velocity component (unit: $m^2s^{-2} \cdot m$), (f) potential
856 temperature (unit: $K^2 \cdot m$), (g) corrected static pressure (unit: $hPa^2 \cdot m$), (h) static pressure
857 (unit: $hPa^2 \cdot m$), and (i) hydrostatic pressure correction (unit: $hPa^2 \cdot m$). The subplot (e) kinetic
858 energy (unit: $m^2s^{-2} \cdot m$) is the sum of (a)-(c). Green lines show the composite curves of the
859 theoretical Markov spectrum and the 5% and 95% confidence curves using the lag 1
860 autocorrelation. The blue (red) reference lines have slopes of -5/3 (-3).

861
862 **Figure 6.** Wavelet power spectrum of GV flight-level aircraft measurement during 5 selected
863 segments (from left to right: J1, J2, J3, M1 and M2) of RF02 in START08: (a) along-track
864 velocity component, (b) across-track velocity component, (c) vertical velocity component, (d)
865 potential temperature, and (e) corrected static pressure. Reference line (black line) shows the
866 cone of influence (COI), and the area outside COI is where edge error becomes important. Black
867 contour lines with dot shading represent 95% significance level based on a red noise background
868 (also see Torrence and Compo 1998; Woods and Smith 2010). The x axis is the same as in Fig.
869 3, including the reversal of segment J3 and M2.

870
871 **Figure 7.** The wavelet cospectrum of (a) $(u'w')_c$, (b) $(v'w')_c$, (c) $(p_c'w')_c$, (d) the quadrature
872 spectrum of $(\theta'w')_q$, and (e) the absolute coherence phase angle of $(\theta'w')_p$ for GV flight-level
873 aircraft measurement during 5 selected segments (from left to right: J1, J2, J3, M1 and M2) of
874 RF02 in START08. Reference line (black line) shows the cone of influence (COI), and the area

Fuqing Zhang 4/25/2015 9:52 AM
Deleted: ,
Fuqing Zhang 4/25/2015 9:52 AM
Deleted: ,
Fuqing Zhang 4/25/2015 9:52 AM
Deleted: , (d) vertical velocity component,
(e)
Fuqing Zhang 4/25/2015 9:52 AM
Deleted: , (f)
Fuqing Zhang 4/25/2015 9:52 AM
Deleted: , (g)
Fuqing Zhang 4/25/2015 9:52 AM
Deleted: ,
Fuqing Zhang 4/25/2015 9:52 AM
Deleted: h
Fuqing Zhang 4/25/2015 9:52 AM
Deleted: .

884 outside COI is where edge error becomes important. Black contour lines with dot shading
885 represent 95% significance level (also see Torrence and Compo 1998; Woods and Smith 2010).
886 The x axis is the same as in Fig. 3, including the reversal of segment J3 and M2. The horizontal
887 black line marks the scale of 50 km.

888

889 **Figure 8.** A relatively good/clean example of mesoscale variations during segment J3 (location
890 250-360 km): (a) along-track velocity component (red; unit in m/s) and vertical velocity
891 component (blue; unit in m/s), (b) across-track velocity component (red; unit in m/s) and vertical
892 velocity component (blue; unit in m/s), (c) along-track velocity component (red; unit in m/s) and
893 across-track velocity component (blue; unit in m/s), (d) corrected static pressure (red; unit in
894 hPa) and along-track velocity component (blue; unit in m/s), (e) corrected static pressure (red;
895 unit in hPa) and across-track velocity component (blue; unit in m/s), (f) corrected static pressure
896 (red; unit in hPa) and vertical velocity component (blue; unit in m/s), (g) potential temperature
897 (red; unit in K) and vertical velocity component (blue; unit in m/s), (h) static pressure (red; unit
898 in hPa) and vertical velocity component (blue; unit in m/s), and (i) hydrostatic pressure
899 correction (red; unit in hPa) and vertical velocity component (blue; unit in m/s). A wavelet-based
900 band-pass filter is applied to extract signals with wavelength from 100 to 120 km for all the
901 above flight variables.

902

903 **Figure 9.** Same as in Fig. 8, but for a relatively bad/noisy example of mesoscale variations
904 during segment J3 (location 560-688 km). The wavelet-based band-pass window is 118-138 km.

905

906 **Figure 10.** Same as in Fig. 8, but for a relatively good/clean example of smaller-scale variations
907 during segment J3 (location 650-750 km). The wavelet-based band-pass window is 32-64 km.

908

909 **Figure 11.** Same as in Fig. 8, but for an example of smaller-scale variations during segment J3
910 (location 680-780 km). The wavelet-based band-pass window is 8-16 km.

911

912 **Figure 12.** (a) The spectrum of corrected static pressure (black), static pressure (blue), and
913 hydrostatic pressure correction (red) based on GV flight-level aircraft measurement during 5
914 selected segments (from left to right: J1, J2, J3, M1 and M2) of RF02 in START08. (b) The
915 spectrum of the square root ratio (see the text for its definition).

916

917

918 **Table 1:** The aircraft statistic parameters of five selected flight segment in RF02 during the
 919 START08 field campaign. Column 1-7 represent the name, the starting time (s), the ending time
 920 (s), the averaged flight height (km), the averaged static pressure (hPa), the total distance, (km),
 921 and the averaged flight speed (m/s) of each selected flight segment.
 922

Flight Segment	Start (s)	End (s)	Averaged Flight Height (km)	Averaged Static Pressure (hPa)	Distance (km)	Averaged Flight Speed (m/s)
J1	2450	5000	11.8	196.9	685.74	268.92
J2	5170	8620	12.5	178.7	908.53	263.34
J3	9120	16850	13.1	162.1	1641.93	212.41
M1	17100	20630	12.6	178.5	950.46	269.25
M2	21500	26430	11.0	227.6	946.90	192.07

923

924

Fuqing Zhang 4/25/2015 9:52 AM
 Deleted: ,

Fuqing Zhang 4/25/2015 9:52 AM
 Deleted: State